JGR Solid Earth

Control of Fault Weakening on the Structural Styles of Underthrusting-Dominated Non-Cohesive Accretionary Wedges

Arthur Bauville[1] , **Mikito Furuichi[1]**, and **Muriel Gerbault[2]**

[1]Center for Mathematical Science and Advanced Technology, Japan Agency for Marin-Earth Science and Technology, Yokohama, Japan, [2]Géosciences Environnement Toulouse (GET), UMR5563(CNRS, IRD, CNES), Observatoire Midi-Pyrénées, Université Paul Sabatier, Toulouse, France

Abstract Underthrusting is a typical process at compressive margins responsible for nappe stacking and sediment subduction. In nature, underthrusting is often associated with weak basal faults, although static mechanical analysis (critical taper theory) suggests that weak basal faults promote accretion while strong basal faults promote underthrusting. We perform mathematical analyses and numerical simulations to determine whether permanent fault weakening promotes or inhibits underthrusting. We investigate the control of permanent fault weakening on the dynamics of a strong-based $((1 - \lambda_b^*)\mu_b \approx (1 - \lambda^*)\mu)$ non-cohesive wedge (μ and μ_b are internal and basal friction, respectively). We control the wedge material strength by a spatially constant fluid overpressure factor (λ^*), and fault strength by a plastic strain weakening factor (χ). First, we use the critical taper theory to determine a mechanical mode diagram that predicts structural styles. Then, we perform numerical simulations of accretionary wedge formation to establish their dynamical structural characteristics. We determine a continuum of structural styles between three end-members which correspond to the theoretical mechanical mode transitions. Style 1 is characterized by thin tectonic slices and little to no underthrusting. Style 2 shows thick slices, nappe stacking, and shallow gravity-driven tectonics. Style 3 displays the complete underthrusting of the incoming sediments, that are exhumed when they reach the backstop. We conclude that in the condition of an initially strong wedge base, permanent fault weakening promotes underthrusting. Thus, this contribution enlightens the control of the dynamic evolution of material properties on the formation of subduction channels, slope instabilities, and antiformal nappe stacks.

1. Introduction

Underthrusting at an active compressional margin is the process by which incoming rocks are thrusted below other tectonic units. In an orogenic context, the underthrusting of tectonic units leads to nappe stacking and thus plays an important role in the burial and exhumation of rocks in mountain belts (e.g., Lugeon, 1902; Merle, 1998; van Hinsbergen et al., 2005). In subduction zones, underthrusted sediments may be incorporated at the base of the accretionary wedge; or they may be dragged with the subducting oceanic plate into the upper mantle where they are partly recycled through arc-magmatism (e.g., Clift & Vannuchi, 2004; Lallemand, 1995; Scholl et al., 1977; von Huene et al., 2004). Sediment underthrusting can lead to the formation of a subduction channel and the basal removal of the upper plate, a process known as subduction erosion. Underthrusting is the dominant process at non-accretionary and erosive margins (Albert et al., 2018; Cloos & Shreve, 1988a, 1988b). For example, Kodaira et al. (2017) estimate that ≈98% of the incoming sediment at the Japan Trench has been subducted. More generally, previous research estimated that non-accretionary margins account for ≈57% of all subduction zones and that even in accretionary margins ≈70% of the incoming sediment may well be subducted (Clift & Vannuchi, 2004; von Huene & Scholl, 1991). Erosive margins develop preferentially when the thickness of incoming sediment is low. Despite being a common process involved in mountain building and subduction zones and that generates seismicity, the mechanics of underthrusting is still incompletely understood.

The mechanics of underthrusting can be approached from the critical taper theory (CTT) (Davis et al., 1983; Dahlen, 1984; Dahlen et al., 1983). The CTT is a mathematical theory based on force balance which predicts that an originally flat-lying plastic material sheared at its base will deform until it reaches a steady state
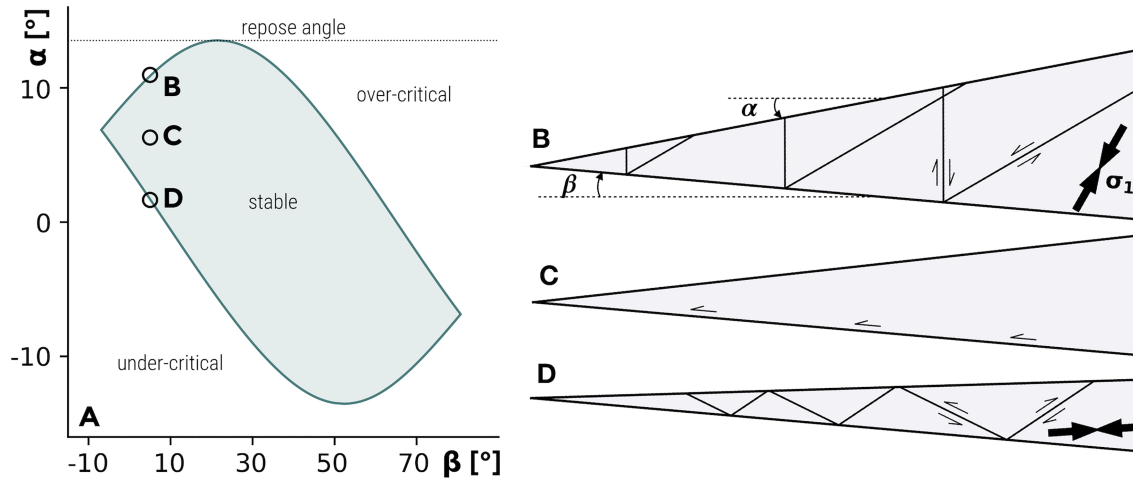
Figure 1. (a) Typical stability field for a wedge with a weak base represented with the surface angle α as a function of the basal angle β. (b–d) Wedge geometry, fault orientation, and orientation of the first principal stress σ_1 for a basal angle of 5° . (b) The extensionally critical wedge, (c) a stable wedge, and (d) the compressively critical wedge. Parameters are friction coefficient ($\mu = 0.6$), basal friction coefficient ($\mu_b = 0.3$), and fluid overpressure factor ($\lambda^* = 33\%$).

wedge shape, the so-called critical taper. The deformation of a pile of sand or snow in front of a bulldozer is a common analog (Dahlen, 1984). We will review the mathematical basis of this theory in section 2.1. Here, we recall some results of this theory in order to set out the reasoning of our present study. For given values of internal friction μ, basal friction μ_b, internal fluid pressure factor λ, and basal fluid pressure factor λ_b there is a limited combination of surface angle (α) and basal angle (β) for which the wedge is stable. The stability conditions, that is, where a wedge deforms only elastically while it slides along its base occur inside the shaded domain of Figures 1a and 1c. The edges of the curve enclosing the stable (α, β) region on Figure 1a correspond to critical taper conditions. In the case where $(1 - \lambda_b)\mu_b < (1 - \lambda)\mu$ (weak base), the upper edge of this curve is the extensionally critical taper characterized by normal faults (Figure 1b), while the lower edge is the compressively critical taper characterized by thrust faults (Figure 1d). In the limit where $(1 - \lambda_b)\mu_b = (1 - \lambda)\mu$ (strong base), the stability domain becomes infinitely thin, that is, a line (Figure 2a). In this particular case, one direction of faulting is parallel to the base which constitutes the ideal condition for underthrusting (Figures 2b–2c). We use the term "neutrally critical taper" to refer to this case.

Contrary to the theoretical prediction that a basal fault needs to be as strong as the wedge material to trigger underplating, natural evidence suggests that plate boundary faults responsible for underthrusting at erosive margins can be very weak. For instance, at the North Chile and South Ecuador erosive margins the middle
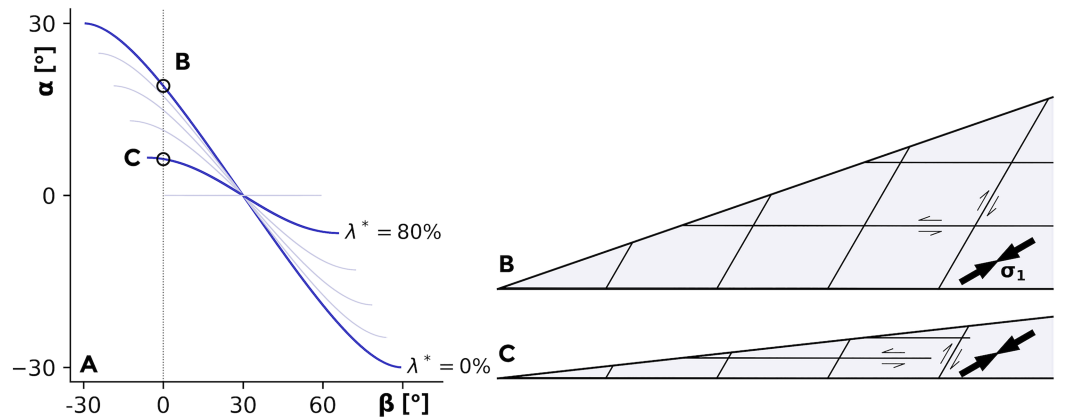
Figure 2. (a) The stability field of wedges with a strong base ($(1 - \lambda_b^*)\mu_b = (1 - \lambda^*)\mu$) is a line. The taper angle is strongly controlled by the fluid overpressure factor λ^*. (b–c) Wedge geometry, fault, and principal stress orientations. σ_1 is oriented at Coulomb angle to the base, since one direction of faulting is parallel to the base. Thus, it constitutes the ideal conditions for underthrusting. Parameters are friction coefficient ($\mu = 0.6$), basal friction coefficient ($\mu_b = 0.3$), and fluid overpressure factor ($\lambda^* = 33\%$).

prisms are typically affected by normal faults which suggest that they are in extensionally critical condition (e.g., Sage et al., 2006; von Huene & Ranero, 2003) and therefore that the basal fault is significantly weaker than the internal wedge strength. The presence of an extensionally critical prism is generally interpreted as the result of a multistep process. First, a wedge with a relatively high taper is built. Then, a reduction of the inner and/or basal effective friction coefficient leads to the taper becoming overcritical. Finally, the wedge deforms to lower its surface angle until reaching the extensionally critical conditions (Cubas et al., 2013; Dahlen, 1984; Wang et al., 2010). Therefore, the presence of normal faults in the middle prism is indicative of a weak plate boundary fault. Gao and Wang (2014) estimated, based on heat flow data inversion that even at erosive subduction margins, that the effective friction coefficient along the plate boundary is less than 0.15.

Wang et al. (2010) proposed that theory and observations can be reconciled by considering variations of the plate boundary strength during the subduction earthquake cycle. In their model, they assume that the basal fault is rate strengthening and therefore that underthrusting occurs during earthquakes when the fault is strong, and normal faulting in the prism occurs in the interseismic period when the fault is weak. However, the results of Gao and Wang (2014) suggest that the section of the plate boundary faults that is below the middle prism at erosive margins may remain relatively weak during earthquakes.

In addition to dynamic strengthening or weakening during earthquakes, faults and plastic shear bands also experience permanent weakening caused by, for example, the evolution of rock fabrics (Tesei et al., 2015), fluid pressure increase (e.g., Hubbert & Rubey, 1959; Terzaghi, 1950; Tobin et al., 1994), gouge formation (Burridge & Knopoff, 1967; Dieterich, 1979; Di Toro et al., 2011; Ruina, 1983; Reches & Dewers, 2005; Vrolijk & van der Pluijm, 1999), and stress rotation (Le Pourhiet, 2013; Marone et al., 1992; Marone, 1995; Vermeer & De Borst, 1984). Previous authors showed that weakening controls the effective inner strength of the prism (Lohrmann et al., 2003; Ruh et al., 2012). Here we investigate the control of permanent fault weakening on underthrusting, by assuming persistent strain-dependent reduction of friction (in contrast to the cyclic properties proposed by Wang et al., 2010). In agreement with previous studies, we confirm that a strong weakening favors the formation of an extensional wedge. A more surprising result is that this condition also favors underthrusting. The new model that we propose predicts the observed occurrence of coeval permanently weak faults, extensional wedges, and underthrusting.

The goal of this contribution is to determine whether permanent fault weakening promotes or inhibits underthrusting. First, we use the critical taper theory to identify possible structural styles triggered by the transition from an initial intact state to a second state where the internal and/or basal faults have been weakened. Second, we perform numerical simulations of deformation of an initially flat layer of plastic material submitted to sandbox-like boundary conditions. Fault weakening was applied to yielded areas using strain softening. The numerical results are consistent with the analytical solution and show a continuum of structural styles ranging from full accretion to full underplating. We discuss the results against analog sandbox experiments and natural examples of underthrusting and gravity collapse.

2. Theoretical Model
2.1. Review of the Critical Taper Theory for a Non-Cohesive Wedge
The critical taper theory was developed through a series of seminal papers in the late 1970s and 1980s (Dahlen, 1984; Dahlen et al., 1983; Davis et al., 1983; Chapple, 1978). The critical taper equations were derived from the equations of stress equilibrium and the Coulomb failure criterion while imposing a shear stress-free condition at the top surface and a critical state of shear stress at the base. In this contribution we propose a simple algorithm to construct the critical taper solution based on results by Lehner (1986). A numerical implementation of this algorithm is given in Appendix B and is available online alongside a set of functions to compute and visualize the solutions of the critical taper equations (Bauville, 2019).

Let us consider a submerged wedge whose surface makes an angle α with the horizontal (positive counterclockwise). The wedge is bounded at the base by a plane of weakness which makes an angle β with the horizontal (positive clockwise) (Figure 1b). The relevant material properties are the densities of the wedge material (ρ) and water (ρ_w), and the friction angles (ϕ) or friction coefficient ($\mu = \tan \phi$) in the wedge and on the basal plane of weakness (ϕ_b, μ_b). For a submerged wedge we also define the generalized Hubbert-Rubey fluid pressure factor in the wedge (λ) and at the base (λ_b).

$$\lambda = \frac{P_f - P_{wc}}{P_{litho} - P_{wc}}, \text{ with} \tag{1}$$

$$P_{wc} = \rho_w g D, \text{ and} \tag{2}$$

$$P_{litho} = \rho_w g D + \rho g H, \tag{3}$$

where P_f is the fluid pressure at a given depth and P_{wc} is the pressure associated with the weight of the water column of height D above the wedge. P_{litho} is the lithostatic pressure, that is, the pressure associated with the combined weight of the water column and the rock column of density ρ and height H. We also define the hydrostatic pressure $P_{hydro} = \rho_w g (D + H)$.

It is convenient to define the fluid overpressure factors λ^* and λ_b^* that measure the fluid pressure in excess of the hydrostatic pressure. It varies from 0 at hydrostatic pressure ($P_f = P_{hydro}$) to 1 at lithostatic pressure ($P_f = P_{litho}$).

$$\lambda^* = \frac{P_f - P_{hydro}}{P_{litho} - P_{hydro}}, \text{ or} \tag{4}$$

$$\lambda^* = \frac{\lambda - \lambda_{hydro}}{1 - \lambda_{hydro}}, \tag{5}$$

where $\lambda_{hydro} = \rho_w / \rho$ is the hydrostatic fluid pressure factor.

Next, we define the effective friction coefficients μ^* and μ_b^* following Wang and Hu (2006)

$$\mu^* = (1 - \lambda^*)\mu, \tag{6}$$

$$\mu_b^* = (1 - \lambda_b^*)\mu_b, \tag{7}$$

and another effective friction coefficient μ_b' following Dahlen (1984)

$$\mu_b' = \frac{\mu_b^*}{\mu^*}\mu. \tag{8}$$

Let us also define the effective surface angle (α') which expresses the ratio of shear stress to surface orthogonal normal stress (Lehner, 1986),

$$\tan \alpha' = \frac{\tan \alpha}{(1 - \lambda^*)}. \tag{9}$$

Finally, we define two intermediate angles (Lehner, 1986) to simplify the final notation.

$$\gamma = sin^{-1}\left(\frac{\sin \alpha'}{\sin \phi}\right), \tag{10}$$

$$\theta = sin^{-1}\left(\frac{\sin \phi_b'}{\sin \phi}\right), \tag{11}$$

where $\phi_b' = \tan^{-1}\mu_b'$.

The sum of the surface and basal angles is called the taper angle. When the gravity forces in the wedge balance the frictional forces on the base the taper angle satisfies (Dahlen, 1984; Lehner, 1986)

$$\alpha + \beta = \psi_b - \psi_0, \tag{12}$$

where ψ_b and ψ_0 are the angles between the direction of the maximum principal stress σ_1 and the base, and the surface of the wedge, respectively. Following Lehner (1986) we construct the critical taper envelope by solving equation (12) for β. The critical taper envelope can be separated in four segments (Figure 3). The two segments in dashed lines represent solutions where the wedge is extensionally critical while the segments in solid lines represent solutions where the wedge is compressively critical. By manipulating equations (9) to (14) of Lehner (1986) we obtain

$$\begin{cases} \psi_b = \frac{1}{2}\left(-\theta - \phi_b' + \pi\right), & \text{for the upper envelope,} \\ \psi_b = \frac{1}{2}\left(\theta - \phi_b'\right), & \text{for the lower envelope.} \end{cases} \tag{13}$$
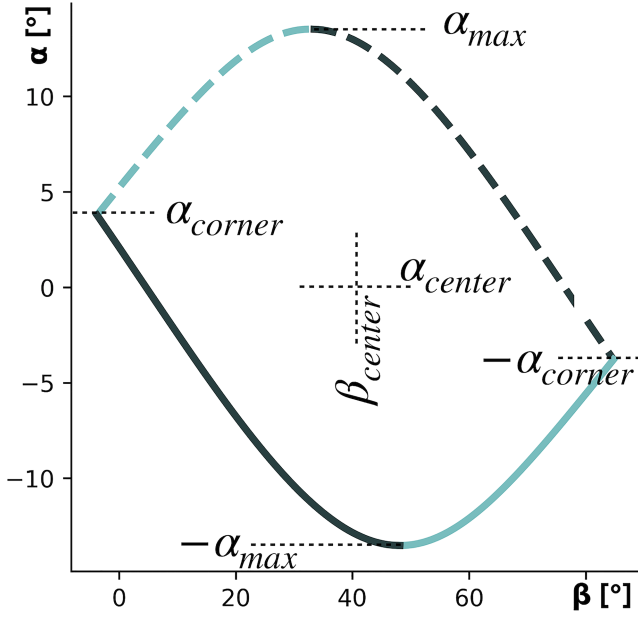
Figure 3. The critical taper envelope is solution of the equation $\alpha + \beta = \psi_b - \psi_0$. In this equation α is the surface angle, β is the basal angle, ψ_b and ψ_0 are the angles between the first principal stress direction and the base or the surface, respectively. One method to construct the critical envelope consists in solving the critical taper equation for β as a function of α in four segments, here highlighted by combinations of line style and color. Dashed lines denote solutions where the wedge is extensionally critical, while solid lines denote solutions where the wedge is compressively critical. Dashed segments share the same formulation of ψ_b, while solid segments share the same formulation of ψ_0.

The upper and lower envelope is subdivided in two segments represented by light or dark colors in (3), with the relationship

$$\begin{cases} \psi_0 = \frac{1}{2}\left(-\gamma - \alpha' + \pi\right), & \text{for light-colored segments,} \\ \psi_0 = \frac{1}{2}\left(\gamma - \alpha'\right), & \text{for dark-colored segments.} \end{cases} \tag{14}$$

Finally, we note that the segments are bounded by values $\alpha = \pm\alpha_{max}$ and $\alpha = \pm\alpha_{corner}$, with

$$\tan \alpha_{max} = \mu^*, \quad and \tag{15}$$

$$\tan \alpha_{corner} = \mu_b^*. \tag{16}$$

A python script implementing this method is given in Appendix B. The implementation has been benchmarked against the graphical solution described in the section "Stable versus unstable wedges" of Dahlen (1984). Also, one can note that the explicit solution for $\psi_b \psi_0$ given in Dahlen (1984) (his equations (9) and (19)) corresponds to the equation for the dark-colored solid segment (Figure 3, equations (13) and (13)).

To better understand the variability of the solution note that the stability domain has a second order rotational symmetry of center $\alpha_{center}, \beta_{center}$ with

$$\alpha_{center} = 0, \tag{17}$$

$$\beta_{center} = \frac{\pi}{4} - \frac{\phi_b'}{2}. \tag{18}$$

The equation of β_{center} has the same form as the equation of the Coulomb angle, that is, the angle at which faults form with respect to the first principal stress, where $\theta_{Coulomb} = \pi/4 - \phi/2$. At the left corner

$$\beta(\alpha_{corner}) = -\alpha_{corner}, \tag{19}$$

and α is maximum when

$$\beta(\alpha_{max}) = \beta_{center} - \alpha_{max} + \frac{\phi - \theta}{2}. \tag{20}$$

2.2. Critical Taper Theory with Fault Weakening

Dahlen (1984) already recognized the strong control that variations in time of the wedge properties $\lambda, \lambda_b, \mu, \mu_b, and \beta$ have on the wedge dynamics. For instance, an initially flat layer of material deforms until it reaches the compressively critical taper. If wedge properties remain constant, it will continue to grow self-similarly. However, if the wedge properties change, it may become either stable, undercritical of overcritical. If the wedge becomes overcritical, then, extensional deformation is triggered, and the wedge taper decreases until it reaches the extensionally critical conditions.

To determine the change in wedge properties necessary to trigger extensional deformation, we consider the evolution of a wedge from an initial intact stage, characterized by the compressively critical surface angle α_{0c}, to a final weakened stage. We introduce the following two functions:

$$\bar{\alpha} = \frac{\alpha}{\alpha_{max}}, \tag{21}$$

$$\Delta\bar{\alpha} = \frac{\alpha_{1e} - \alpha_{0c}}{\alpha_{max}}, \tag{22}$$

where α_{1e} is the extensionally critical surface angle in the final (weakened) stage. The wedge becomes extensionally critical when $\Delta\bar{\alpha} <= 0$.
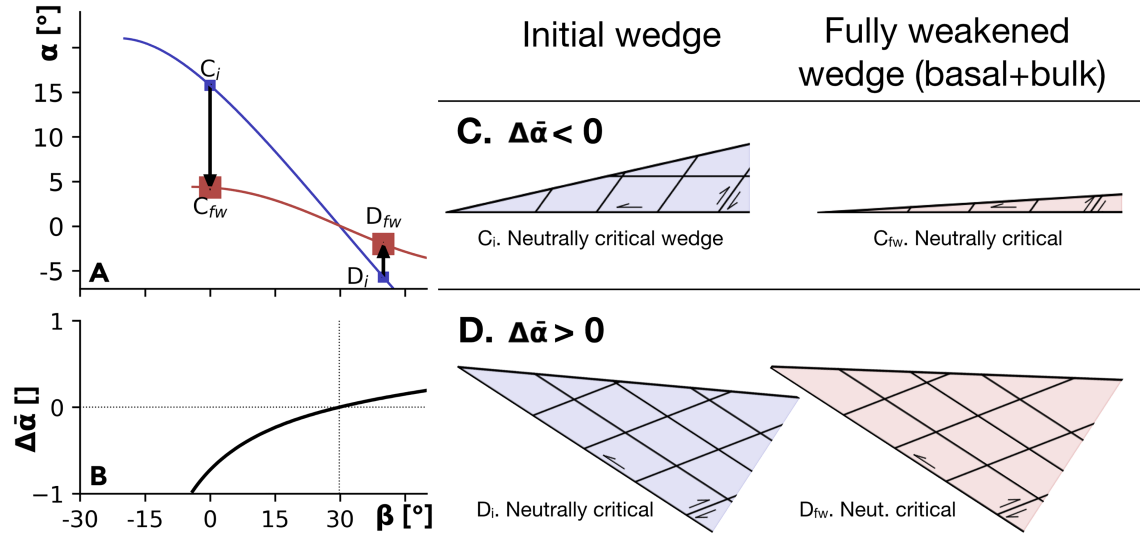
Figure 4. (a) Stability lines of a strong-based ($\mu_b^* = \mu^*$) wedge (blue line) a fully weakened wedge (red line). The arrow represents the change in surface angle as a consequence of the weakening. (b) Graph of $\Delta\bar{\alpha}$ as a function of β. (c–d) Examples of wedge geometry and fault orientation of the initial and fully weakened wedge in the case where $\Delta\bar{\alpha} < 0$ (c) and $\Delta\bar{\alpha} > 0$ (d). Parameters are $\mu = 0.6$, $\lambda^* = 33\%$, and $\chi = 80\%$.

In this section we systematically examine the control of fault weakening, that is, temporal variations of μ and/or μ_b, on the structural style of accretionary prisms by means of the function $\Delta\bar{\alpha}$. This analysis only makes use of steady-state solutions and therefore cannot describe the change of kinematics. In a later section of this paper we show numerical solutions that are fully dynamic and adequately describe the kinematics. As we will show later, this simple analysis captures the first order behavior of the dynamic numerical simulations. Since we focus on the modalities of underthrusting we restrict the initial conditions to strong-based cases which is theoretically the ideal condition for underthrusting, that is, $\mu_b^* = \mu^* = \mu_0^*$, where μ_0^* is a reference effective coefficient of friction (Figure 2). When the wedge is pushed at the rear, it will deform by the formation localized zones of deformation such as faults and plastic shear bands. These localized zones of deformation are generally weaker than the intact material (e.g., Terzaghi, 1950; Tesei et al., 2015; Vermeer & De Borst, 1984). To quantify the impact of fault formation on the wedge dynamics we introduce the weakening factor χ

$$1 - \chi = \frac{\mu_f^*}{\mu_0^*}, \tag{23}$$

where μ_f^* is the effective friction coefficient of the material inside the fault or shear band.

The critical taper theory predicts the orientation of faults but not their location. As a starting point, it is useful to consider two end-member cases which both evolve from the same initial stage defined above (i.e., $\mu_b^* = \mu^* = \mu_0^*$ initially). One extreme case corresponds to a "fully weakened wedge," where the wedge and its base are pervasively faulted, that is, $\mu_b^* = \mu^* = \mu_f^*$. The other extreme case is represented by a "basally weakened wedge," where the basal fault is weakened but faulting within the wedge does not lead to a significant strength decrease. Thus, $\mu_b^* = \mu_f^*$, and $\mu^* = \mu_0^*$.

2.2.1. Fully Weakened Wedge

Figure 4a shows the stability domains of the initial stage (blue line) and a fully weakened wedge (red line). In both cases $\mu^* = \mu_b^*$, therefore, as shown in Figure 2, the stability domains are lines. The function $\Delta\bar{\alpha}$ is graphed in Figure 4b. When $\Delta\bar{\alpha} < 0$, the final taper angle is smaller than the initial one (Figure 4c), while when $\Delta\bar{\alpha} > 0$, the final taper angle is larger than the initial one (Figure 4c). In the fully weakened wedge case, the base of the prism is always one of the two possible sliding/faulting directions, which by definition are oriented at the Coulomb angle $\pm(\pi/4 - \phi/2)$ from the most compressive stress σ_1. σ_1 is correspondingly inclined with respect to the base.

2.2.2. Basally Weakened Wedge

We now consider a basally weakened wedge, that is, $\mu^* = \mu_0^*$ and $\mu_b^* = \mu_f^*$. A strong-based wedge forms in the limit where $\chi \approx 0\%$. At the opposite, when $\chi \approx 100\%$ there is no frictional resistance at the base (i.e.,
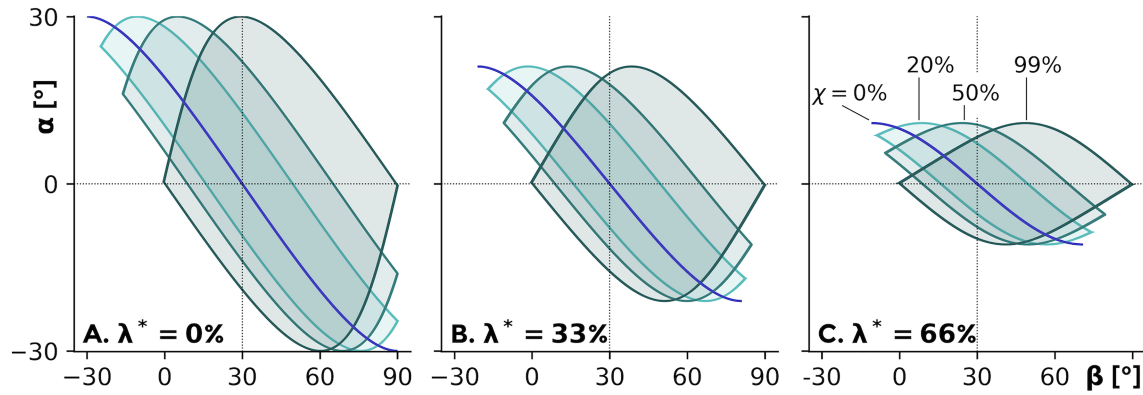
Figure 5. Stability fields for a variety of basally weakened wedges illustrating the sensitivity to variables χ and λ^*. $\lambda^* = \lambda_b^*$.

free slip, Figure 5). The case where $\lambda^* = 0\%$ corresponds to a dry wedge or a submarine wedge in which the fluid pressure is hydrostatic. In the opposite case where $\lambda^* = 100\%$, the fluid pressure equals the lithostatic pressure, and therefore, the internal strength of the wedge goes to zero. Then, the wedge material cannot support any lateral stress caused by the topography, and therefore, $\alpha = 0°$.

Figure 6a shows the stability domains of the initial wedge (blue line) and a basally weakened wedge (green area). The function $\Delta\bar{\alpha}$ is graphed in Figure 6b. When $\Delta\bar{\alpha} < 0$, transitioning from the initial to the weakened state causes the taper to become overcritical, and therefore, extensional deformation is triggered. Consequently, the surface angle is reduced down to the extensionally critical taper conditions of the weakened wedge (Figure 6c). The black arrow illustrates this process. On the other hand, when $\Delta\bar{\alpha} > 0$, then the basally weakened wedge is stable, and therefore, there is no modification of the surface angle (Figure 6d).

Figure 7a shows a graph of $\bar{\alpha}$ as a function of $(1 - \chi)$ for $\beta = 0$ and $\lambda^* = 0$. The green area corresponds to the stability domain of the weakened wedge, while the blue line indicates the surface angle of the intact wedge (i.e., α_{0c}, in equation (22)). The dashed and solid green lines indicate the compressional and extensional critical state solutions, respectively. Thus, $\Delta\bar{\alpha}$ is the signed distance between the solid green and blue lines. To illustrate the dependence of the surface angle on χ we show two examples. Decreasing the strength of the basal fault up to $\chi = 50\%$ should have no incidence because the wedge built at the initial angle remains stable (red arrow in Figure 7a), that is, the wedge deforms only elastically and slides on its base. This is specifically true for all values of χ for which $\Delta\bar{\alpha}$ is positive (red arrow in Figure 7a). On the other hand, if
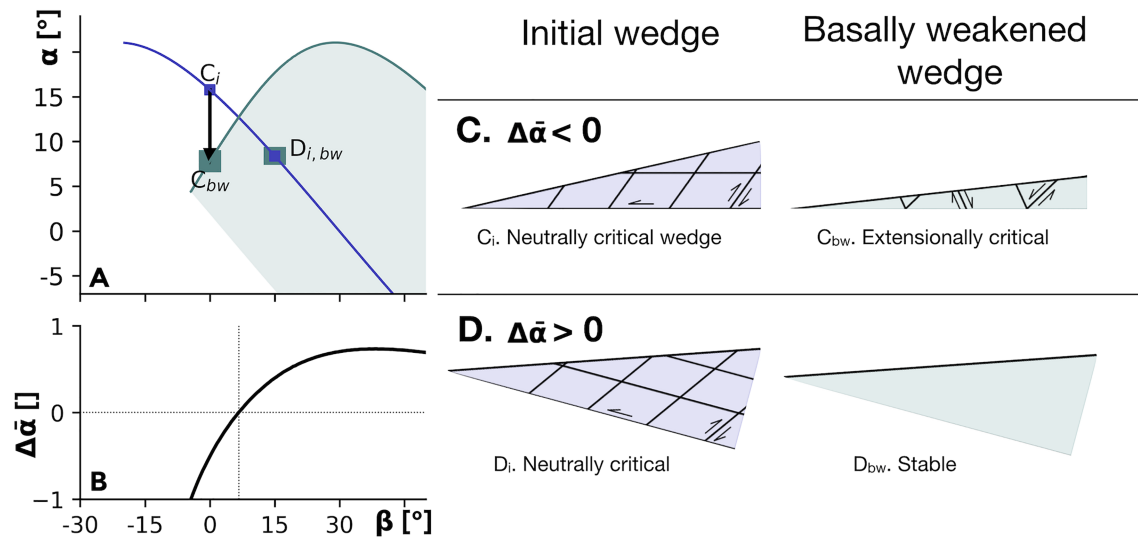
Figure 6. (a) Stability field of a strong-based ($\mu_b^* = \mu^*$) wedge (blue line) and basally weakened wedge (green area). The green line outlines the extensionally critical taper solutions of the basally weakened wedge. The arrow represents the change in surface angle as a consequence of the weakening. (b) Graph of $\Delta\bar{\alpha}$ as a function of β. (c–d) Examples of wedge geometry and fault orientation of the initial and basally weakened wedge in the case where $\Delta\bar{\alpha} < 0$ (c) and $\Delta\bar{\alpha} > 0$ (d).
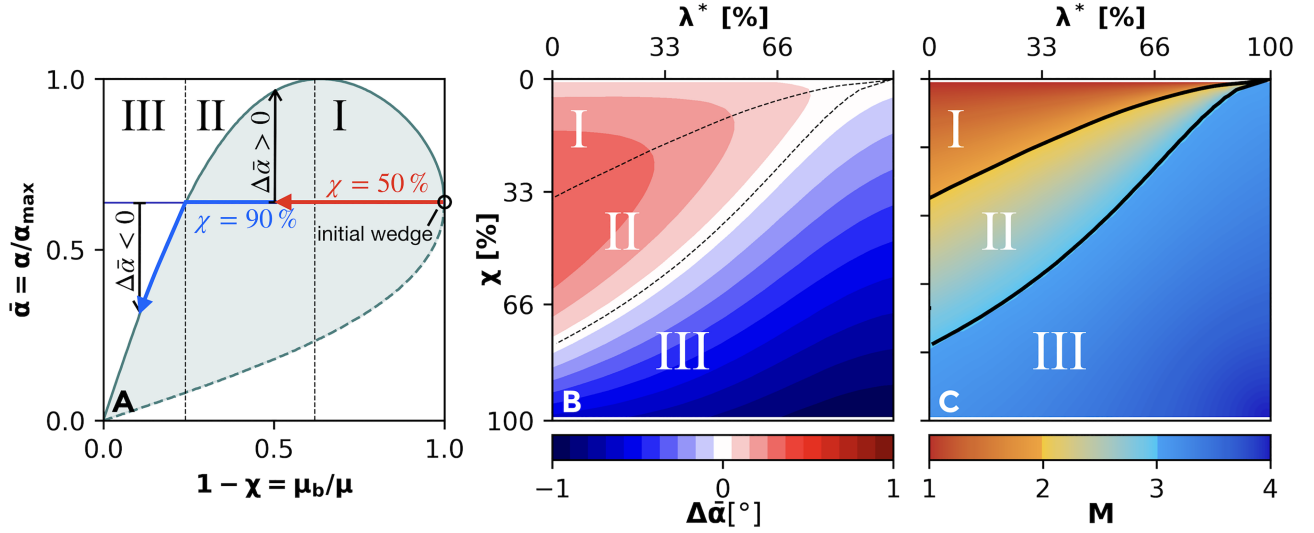
Figure 7. (a) Stability diagram of a basally weakened wedge in the space $\bar{\alpha}$ versus $(1 - \chi)$ illustrating the control of χ on the surface angle of a basally weakened wedge. The wedge has value $\beta = 0$ and $\lambda^* = 0$. The dark blue line indicates the surface angle of the intact wedge. The blue and green arrows indicate a hypothetical transition path from an initally intact wedge to a basally weakened wedge. The dashed and solid green lines indicate the compressive and extensionally critical surface angles, respectively. The green area delimits the domain where the wedge is stable. I, II, and III indicate three mechanical modes separated by dashed lines. (b) Contour plot of $\Delta\bar{\alpha}$ as a function of the fluid overpressure factor λ^* and the weakening factor χ. (c) Contour plot of the mode number function M assigned as a function of the distance to mechanical mode transitions (black lines).

the basal strength is decreased up to $\chi = 90\%$ the initial surface angle must become unstable; therefore, the wedge becomes extensionally unstable. This is specifically true for all values of χ for which $\Delta\bar{\alpha}$ is negative (red arrow in Figure 7a). A similar analysis was proposed by Willett (1992) and will be discussed later in section 4.1.

Figure 7b shows a contour plot of $\Delta\bar{\alpha}$ as a function of χ and λ^*, for a constant $\beta = 0$. Based on the value and variation of function $\Delta\bar{\alpha}$, we can identify three regions or mechanical modes. The boundary between modes II and III is the zero crossing of function $\Delta\bar{\alpha}$, while the boundary between modes I and II corresponds to a "ridge" of $\Delta\bar{\alpha}$, that is, a linear local maximum in the represented space. In modes I and II $\Delta\bar{\alpha} > 0$. In mode I $\Delta\bar{\alpha}$ increases with increasing χ and is mostly independent of λ^*, while in mode II, $\Delta\bar{\alpha}$ decreases with increasing χ and and λ^*. In mode III $\Delta\bar{\alpha} < 0$ and it decreases with increasing χ.

In modes I and II $\Delta\bar{\alpha} > 0$, therefore, the initial wedge is predicted to be stable in the weakened conditions (as in Figure 6d). On the contrary, in mode III the initial wedge is overcritical and must deform to reach the extensional critical taper of the weakened wedge (Figure 6c). The critical taper theory alone does not predict a structural style difference between modes I and II. To overcome this shortcoming and to obtain more information about the structural style of underthrusting-dominated wedges, in the following section we present a set of numerical simulations that cover the parameter space presented in Figure 7a. $\Delta\bar{\alpha} > 0$ does not increase monotonically across the parameter space. Therefore, to ease the representation of results in the following sections, we introduce the monotonic function "mode number" M (Figure 7c). $M = 1$ at $\chi = 0$; $M = 2$ at the transition between the modes I and II; $M = 3$ at the transition II/III, and $M = 4$ at $\chi = 100\%$ and $\lambda^* = 100\%$. M is interpolated linearly between mode transitions to cover all the parameter space.

3. Numerical Simulations

In this section, we first give an overview of the numerical methods and initial configuration before presenting the simulation results. The numerical results are presented in the context of the theoretical predictions.

3.1. Methods
3.1.1. Numerical Method
The numerical algorithm solves the Stokes equations that describe the flow of rocks over a geological time scale. The software is based on finite-difference marker-in-cell method (Harlow & Welch, 1965;
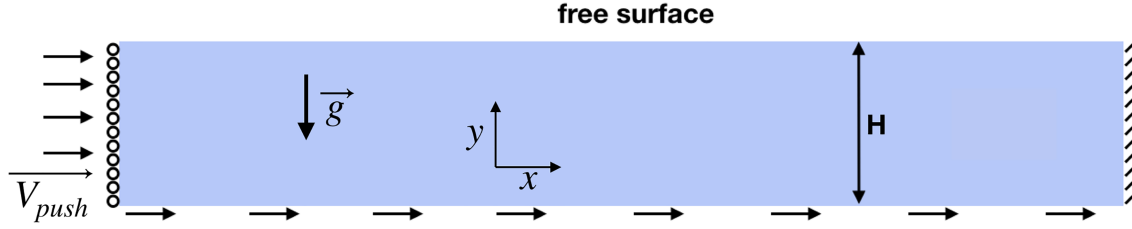
Figure 8. Schematic diagram of the initial configuration and boundary conditions. Boundary conditions are (top) free surface (sticky air); (right) no slip; (left) free slip and constant horizontal velocity Vx = Vpush; (bottom) vertical velocty Vy = 0, horizontal velocity Vx = Vpush.

Gerya & Yuen, 2003). All invariants are computed on a staggered grid. The system of equations is solved for v_x, v_y and P using the implicit direct solver PARDISO v6.0.0 (De Coninck et al., 2016; Kourounis et al., 2018; Verbosio et al., 2017). The viscous term is effectively switched off by using a very high viscosity. We chose the time step size such that it takes at least one to two time steps to build enough elastic stress to reach the yield stress. The plastic rheology follows a non-associative flow rule. We describe the governing and constitutive equations in details in Appendix A.

Here, we give a brief description of the strain weakening algorithm. The yield stress is defined by the Mohr-Coulomb relation,

$$\tau_y = Ccos(\phi) + (1 - \lambda)(P - P_{wc})sin(\phi), \tag{24}$$

where C is cohesion, ϕ is the friction angle, λ is a fluid pressure factor, P is the pressure, and P_{wc} is the weight of the overlying column of water. The standard yield function for a Mohr-Coulomb failure criterion is defined as $F = \tau_{II} - \tau_y \leq 0$, where τ_{II} is the second invariant of the stress tensor. Here instead the yield function is defined according to the weakening factor χ, such that

$$F = \tau_{II} - (1 - \chi w(\epsilon_p))\tau_y, \tag{25}$$

ϵ_p is the second invariant of the cumulated plastic strain, and $w(\epsilon_p)$ is a piecewise linear weighting function which takes values 0 for $0 < \epsilon_p < 0.5$ (no weakening) and 1 for $\epsilon_p > 1$ (maximal weakening). $w(\epsilon_p)$ increases linearly from 0 to 1 for $0.5 < \epsilon_p < 1$.

3.1.2. Model Configuration

The model configuration mimics a 2D sandbox experiment (Figure 8). We set a homogeneous layer of sediment of constant thickness of H. For all simulations the size of a single cell is $d_x = d_y = H/64$. The basal angle is $\beta = 0°$ all along the present study. The layer is dragged from below and pushed at the left boundary against a fixed backstop (right boundary). At the left boundary the horizontal velocity $v_x = v_{push}$, and the vertical velocity v_y remains such that the shear stress $\sigma_{xy} = 0$ (free slip). At the bottom boundary $v_y = 0$ and $v_x = v_{push}$. At the top boundary of the numerical domain, $\sigma_{xy} = 0$ and v_y balances the inbound flow from the left boundary. At the right boundary $v_x = v_y = 0$ (no slip). Displacement along the right boundary is accomodated either by backthrust faults or by plastic shear zones at the boundary, developing early in the simulation. This equivalence has been verified a posteriori by the agreement between the numerical model and the analytical solution wherein a stress condition is specified at the boundary (Buiter et al., 2006, 2016). On top of the sediment layer we set a layer of sticky water, that is, a layer of very low viscosity with a density of 1,000 kg/m³, such that the surface of the sediment layer is effectively shear stress-free (i.e., vertically loaded free surface, Crameri et al., 2012). The sediment has a density of 2,500 kg/m³, and the shear modulus is such that in the initial conditions, the strain necessary to reach the yield stress at a depth H (i.e., which corresponds to the base of the model at the beginning of the simulation) is $\tau_y/(2G) = 1\%$. The friction angle is $\phi = 30°$. In the absence of cohesion, stress vanishes at the surface which can cause a very large velocity. To avoid this situation, we use a small value of cohesion. For each simulation, this value is chosen such that the thickness of the cohesive boundary layer is $H_c = H/32$, that is, two cells, with

$$H_c = \frac{C}{(1 - \lambda)\rho g \mu}, \tag{26}$$

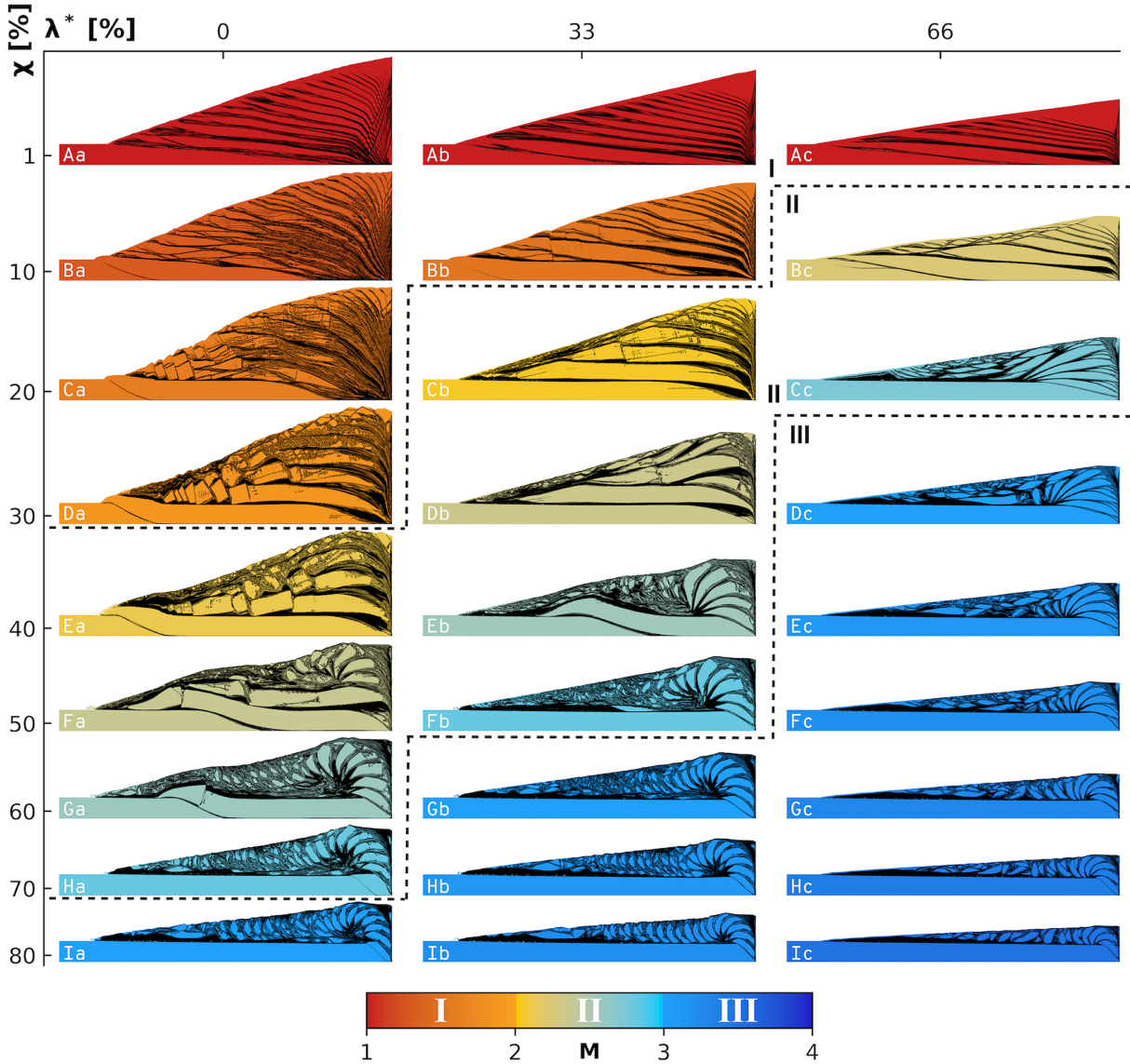where g is the acceleration of gravity.

Figure 9. Wedge geometry (color) and fault geometry (black) for a set of 27 simulations with systematic combinations of χ and λ^*. The wedge material is color-coded according to the theoretical mode number M. Colors are darkened according to plastic strain. The theoretical boundary between modes is indicated by dashed lines.

3.2. Results
3.2.1. Systematic Analysis

Figure 9 presents a set of 27 numerical simulations for $\beta = 0$, $\chi = 1, 10, 20, 30, 40, 50, 60, 70, 80\%$ and $\lambda^* = 0, 33, 66\%$. Each simulation is shown at a different time such that the front of the wedge (i.e., its leftmost extent) is at a similar position and the surface is close to a stable taper for each simulation. The wedge material is colored according to the theoretically determined mode number M. Zones of high plastic strain, that is, faults, are shaded in black. The axes and the colormap are the same as in Figure 7b. Below we use the term tectonic slice or nappe to describe a large sliver of sediment bounded by two parallel faults. First, we can define three archetypal tectonic styles.

Style 1 ($M \approx 1$) is characterized by oblique closed spaced long thrusts that define a stack of thin slices (Figures 9Aa–9Ac). Style 2 ($M \approx 2$) is characterized by nappe stacking with nappes as thick as the incoming sediment. There is a highly deformed region near the surface similar to a slope apron (Figures 9Ea, 9Db, and 9Bc). Style 3 ($M \approx 3$) is characterized by an intensely deformed prism overlaying undeformed incoming sediments. The prism is composed of a rear region with short tectonic slices arranged in a spiral fashion, and a frontal region where those slices have been reworked by extensional tectonics (Figures 9Ia, 9Gb, and 9Dc).
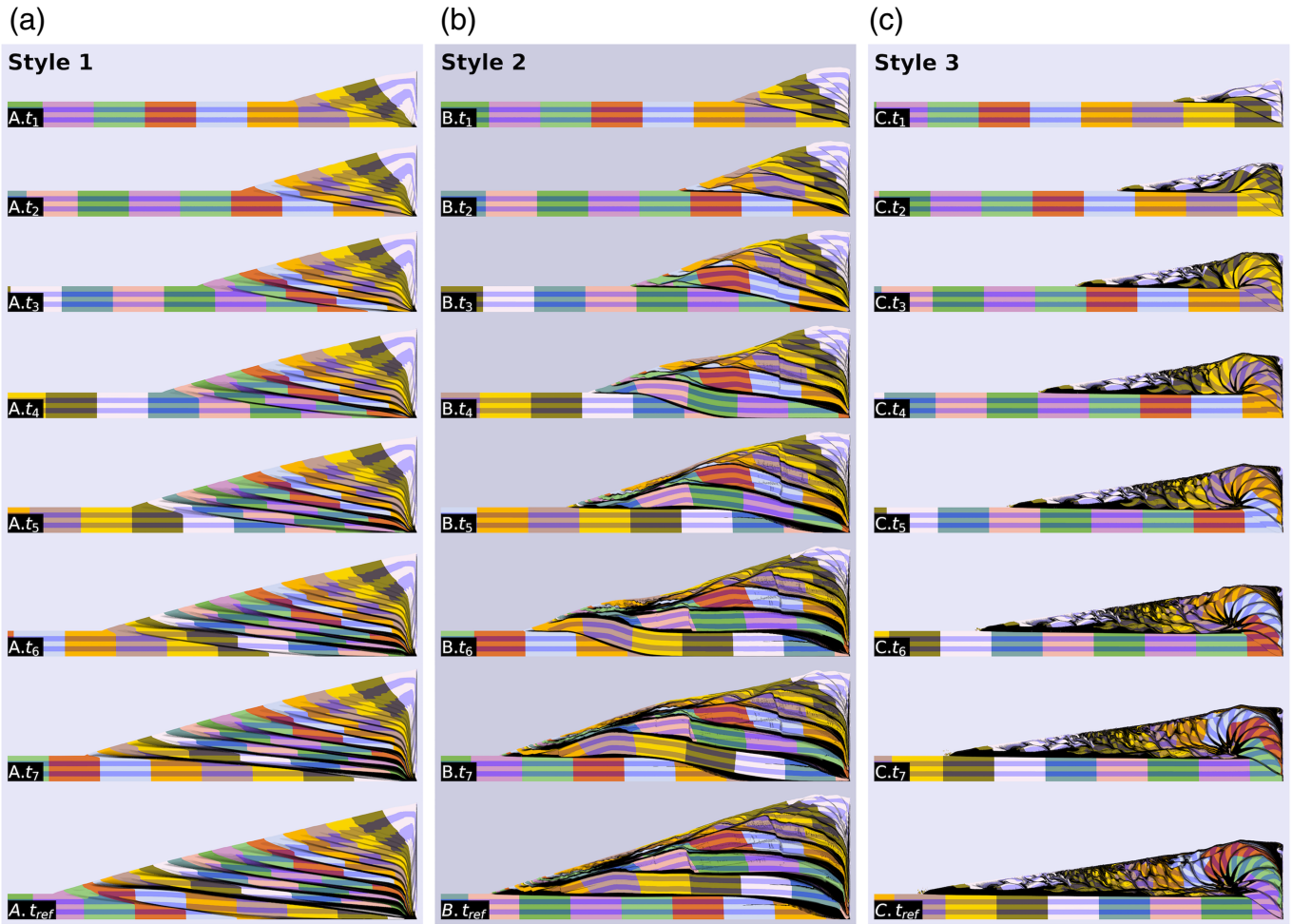
Figure 10. Wedge geometry (colors) and fault geometry (black) of the three simulations archetypal of the tectonic styles. Colors are passive markers of the deformation and are darkened according to plastic strain. $\lambda^* = 33\%$ for all simulations. (a) Style 1, $\chi = 1\%$; (b) Style 2, $\chi = 20\%$; and (c) Style 3, $\chi = 60\%$.

Simulations with intermediate values of M have tectonic styles that share characteristics with the bracketing archetypal styles. Simulations with $1 < M < 2$ are characterized by less well-defined thrust planes with anastomosing faults (Figures 9Ba and 9Bb), and thicker tectonic slices (Figures 9Ba and 9Ca). Simulations with $2 < M < 3$ feature a combination of the long tectonic slices characteristic of Style 2 and the short spiraling slices characteristic of Style 3 (e.g., Figures 9Fa, 9Ga, and 9Eb). The intensity of tectonics also increase gradually from $M = 2$ to $M = 3$ (e.g., Figures 9Ea–9Ha). From $M = 3$ to $M = 4$ the distinction between the front and rear sections of the wedge tends to disappear as the extensional reworking the of the tectonic slices decreases in efficiency. An archetypal Style 4 could have been defined, corresponding to the case $\chi = 100\%$ and a top surface slope parallel to the base.

Simulations with the same mode number M but different combinations of χ and λ^* share many characteristics but also show differences. In simulations where $\lambda^* = 0\%$ and $1 < M < 2$, tectonic nappes are internally faulted (Figures 9Ba–9Da). The frontal part of the prism can also be reworked by normal sense faulting in a domino tectonics fashion (Figures 9Ba and 9Ca). Simulations where $\lambda^* = 33\%$ show significantly less internal faulting of the slices (Figure 9Cb), and simulations where $\lambda^* = 66\%$ do not show any. The simulation where $\chi = 10\%$ and $\lambda^* = 66\%$ (Figure 9Bc) is classified as Style 2 but does not show the characteristic thrusts parallel to the base since the simulation is shown at a relatively early and immature stage. For comparison, in the simulation where $\chi = 20\%$ and $\lambda^* = 33\%$ (Figure 9Cb), the earliest tectonic slices (highest in the pile) are also not parallel to the base. We consider simulations at $\lambda^* = 33\%$ and $\chi = 1\%$, $\chi = 20\%$ and $\chi = 60\%$ to be the most archetypal of Styles 1, 2, and 3, respectively. Therefore, in the following sections, we focus on these three simulations.
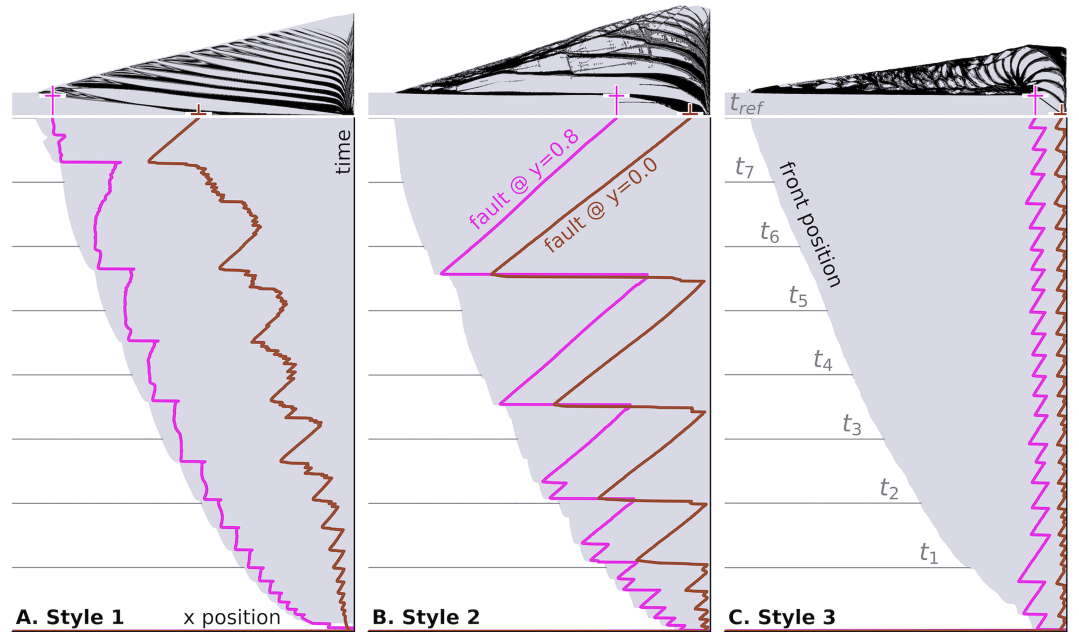
Figure 11. Horizontal position of the forelandmost (i.e., leftmost) fault as a function of time. The wedge and fault geometry of the three simulations at t_{ref} are reproduced above the graph. $\lambda^* = 33\%$ for all simulations. (a) Style 1, $\chi = 1\%$; (b) Style 2, $\chi = 20\%$; and (c) Style 3, $\chi = 60\%$.

3.2.2. Time Evolution of End-Members: Geometry

In the previous section, we described the geometry of tectonic structures qualitatively at a given time. In this section, we describe the evolution of structures in time, and we attempt to characterize them furthermore by monitoring the position of faults and the surface slopes through time.

In Style 1 a new thrust is recurrently formed, connecting the front of the prism to the bottom right corner of the box (Figure 10a). These frequent thrusts define thin tectonic slices. Since the frontal thrusting frequently occurs the surface angle appears relatively constant, and the surface is relatively planar. At a later stage (Figure 10, A.t_{ref}) the rear segment of the frontal thrust runs along the base of the sediment.

In its early stage, Style 2 is similar to Style 1 with new faults cutting the sediment obliquely to connect the front of the wedge to the corner of the box (Figure 10, B.t_1). However, from time t_2 the full sediment thickness is incorporated into nappes. For instance, the purple material is incorporated down to its base in the lowest tectonic slice (Figure 10, B.t_2). The sequence from time t_5 to t_{ref} exemplifies the creation of a tectonic nappe (Figure 10, B.t_6–B.t_{ref}). A frontal thrust appeared slightly before t_6. At t_6 the incoming material is indenting into the material of the nappe. As a consequence, the nappe material is carried up over the ramp formed by the former frontal thrust and the incoming material is underthrusted below. Figure 10 (B.t_7) shows a typical flat-ramp-flat geometry. At t_{ref} the former frontal thrust has reached the backstop. The nappe is completely uplifted, and a new frontal thrust will form soon after to incorporate more material in the wedge. Superficial collapse starts being active from t_2, with recurrent normal faulting over shallow depths. The slope apron keeps on developing until t_{ref}, although its thickness remains fairly constant.

The dynamics of Style 3 can be described in three stages. In the first stage (Figure 10, C.t_1–C.t_2), incoming sediments are faulted to form tectonic slices that are exhumed against the backstop. The exhumed slices are cut again by normal faults. An upper wedge made of normal faulted tectonic slices forms. In the second stage (Figure 10, C.t_3–C.t_5), normal faults do not cut through the entire wedge but affect only a restricted region near the surface. Tectonic slices are exhumed and push toward the front of the upper wedge without being completely normally faulted. The stacked nappes are arranged in a spiral fashion. In the first two stages, the paleo-surface of the incoming sediments constitutes the base of the wedge. In the third stage (Figure 10, C.t_6–C.t_{ref}) a new décollement forms within the wedge to become the new base of the wedge. The new décollement dips toward the foreland, $\beta \approx -4°$ at t_7 and $\beta \approx -2.5°$ at t_{ref}. The most striking feature of Style 3 is the contrast between the intensely deformed wedge and the undeformed incoming sediment
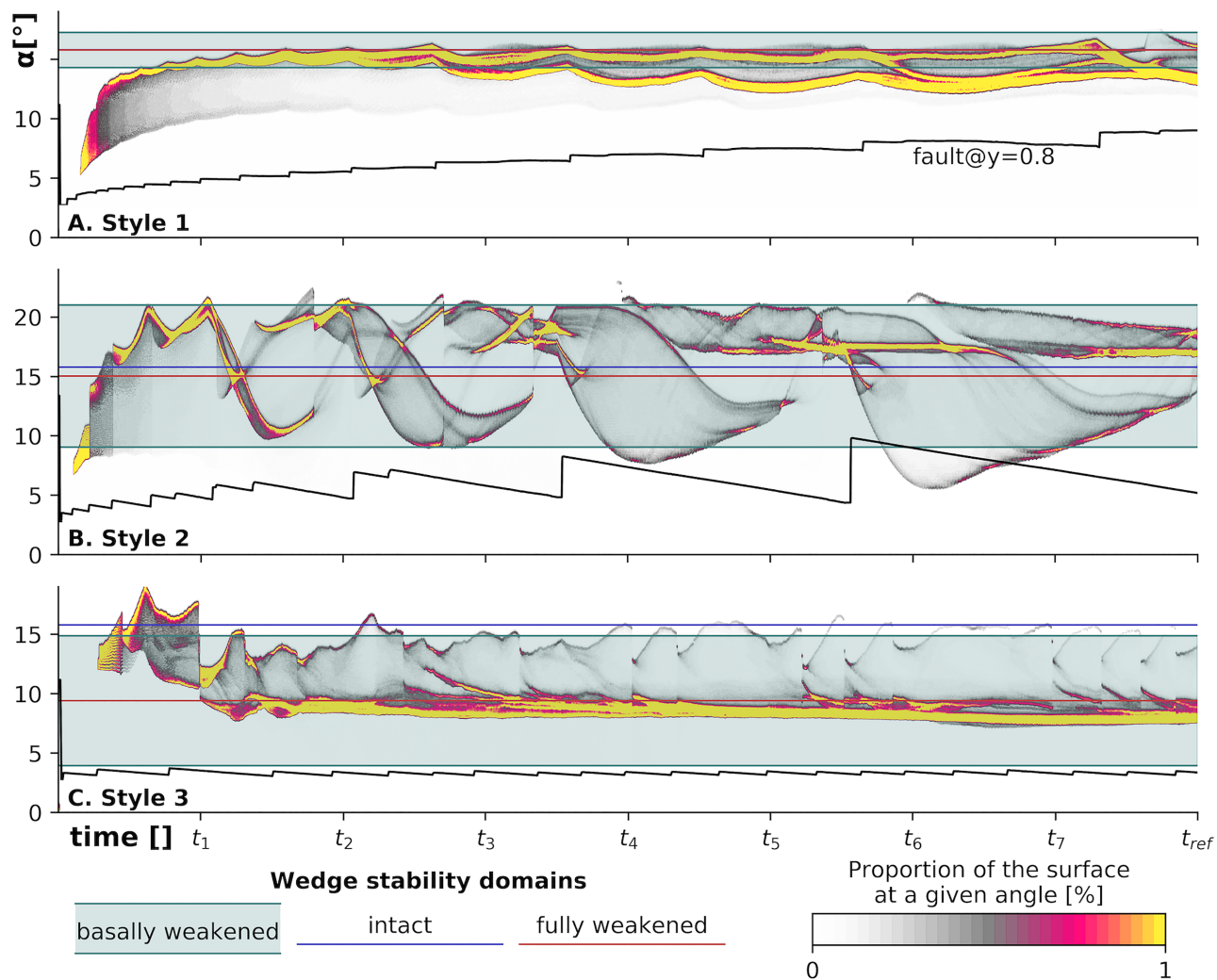
Figure 12. Evolution of the surface angle as a function of time. The colors code for the peak intensity of the surface angle histogram computed for each simulation time step. The theoretical stability range of the basally weakened wedge, intact wedge, and fully weakened wedge are also represented. $\lambda^* = 33\%$ for all simulations. (a) Style 1, $\chi = 1\%$; (b) Style 2, $\chi = 20\%$; and (c) Style 3, $\chi = 60\%$.

pile that is underthrusted below it. Movies of the evolution of the geometry and surface angles of these three simulations are available in supporting information Movies S1–S3.

3.2.3. Time Evolution of End-Members: Faults' Position

In the previous section, we described the geometry of the wedge qualitatively. In the following two sections we characterize the structural style by monitoring scalar values through time. The values we use are the outermost fault position at a given depth (Figure 9), and the surface angle (Figure 10).

Figure 11 shows a graph of the horizontal position of the forelandmost (i.e., leftmost) fault at a given depth (x-axis) as a function of time (y-axis). The wedge geometry and fault geometry of each simulation are represented above the graph at t_{ref} for reference. We graphed the fault position at depth $y = 0.8$ (magenta line) and $y = 0.0$ (brown line). We term these positions, shallow fault position, and basal fault position, respectively. The grayed area in the graph corresponds to the area to the right of the wedge's front. The times t_1 to t_{ref} indicated by gray lines correspond to the time steps shown in Figure 10.

In Style 1, the shallow fault position always remains close to the front position (Figure 11a). Sudden variations in the fault position indicate the formation of a new fault in a more frontal position. The basal fault position marks the same cycle of new fault formation and additional small oscillations. The basal fault position remains close to the backstop until t_2, after which the basal fault position gradually becomes closer to the front. Through the oscillation cycle, the basal fault's position never returns toward the backstop. It means that through time an increasing portion of the base is permanently faulted.

In Style 2, there are cycles where a new fault is formed and then pushed toward the back by incoming sediment (Figure 11b). Once the basal fault position reaches the backstop, a new fault forms. When the new fault forms the shallow fault position is at the front, and the basal fault position is a bit behind. This configuration expresses that when a new fault forms, the fault develops at the base forming a basal décollement from which a frontal thrust steps up (see also B.t_6). At the beginning of the cycle almost all the base is faulted, while at the end, none of it is.

In Style 3, both the shallow and basal front position remain close to the backstop. Similarly to Style 2, a new fault is created when the basal position reaches the backstop. In Styles 1 and 2 the most frontal position of both the shallow and basal fault position follows the advance of the front. However, in Style 3 the position of the fault is independent of the position of the front. The position of the faults near the backstop reflect the regular formation of short tectonic slices.

3.2.4. Time Evolution of End-Members: Surface Angle

Figure 12 presents the time evolution of surface slope for the three end-member simulations. For each time step, the figure presents a histogram of surface slopes. The intensity of the peaks of the histogram is color-coded. To construct this graph, at a given time step we measure the slope at all cell centers defining the surface by performing a least squares regression over topography points over a width $0.5H$ before and after the cell considered. Then, we construct the histogram of the surface slopes at a given time step. The final graph is composed of many histograms, one for each time step, shown next to each other. We also represent the graph of the shallow fault position (fault@$y = 0.8$), given here without scale, to inform the reader on the relation between the surface slope and faulting activity. Over each graph we represent the theoretically determined stability domains of the intact basally weakened and fully weakened wedge. The intact wedge stability domain is a line identical for all simulations. The weakened wedges stability domains are controlled by χ and λ^*, and therefore, they are different for each simulation.

This graph offers a representation of the distribution of local surface slopes in the wedge. Because of the distribution of faults, the mechanical properties (e.g., basal friction) are not homogeneous, and therefore, the slope distribution is often multimodal. The link between multimodal slope distribution and basal faulting can also be observed in Figure 10 (t_4 and t_6).

Style 1 shows first a period of slope increase accompanied by oscillations associated with fault activity (Figure 12a). Around time t_2 the slope becomes asymptotic toward the intact or the fully weakened stability line. Note that since $\chi = 1\%$ both lines nearly overlap. After time t_3 the distribution is bimodal. Part of the wedge oscillates around the intact stability line. Another part of the wedge shows oscillations which peak at the compressively critical state of the basally weakened wedge (i.e., the lower envelope of the green domain). The peak of the oscillations coincides with the formation of a new frontal thrust. Looking back at the wedge geometry (e.g., Figure 10, A.t_7) we observe that the bimodal distribution arises from the convex upward surface. Indeed, the surface slope of the forelandmost half of the wedge is a few degrees steeper than the rearmost half. This dichotomy is likely a consequence of the rearmost part of the base always being faulted, that is, weakened, as shown in Figure 11a.

Style 2 also shows first a period of slope increase that stops before time t_1 when the slope reaches the extensionally critical condition (Figure 12b). At time t_1 the first event of décollement propagation and frontal thrust formation occurs (see also Figure 11b). This faulting event triggers a rapid decrease of the surface slope. Up to now, the slope distribution was unimodal. However, after the slope has decreased to about the level of the intact wedge stability line between time t_1 and t_2, the distribution becomes bimodal. Part of the wedge's slope continues to decrease until it comes close to the compressively critical state, while another part of the wedge increases until it reaches the extensionally critical state. Each major faulting event triggers similar patterns. This multimodal distribution is also clear in, for example, Figure 10 (B.t_3–B.t_7). As in Style 1, the frontal part of the prism is steeper than the rear part. It appears clear that the landslide type surface tectonics coincides with the steeper portions of the wedge and must be triggered when the local surface slope reaches the extensional condition. Although the slope distribution is always multimodal, after time t_5 it becomes clear that some peaks in the distribution become asymptotic. At the end of the simulation, the asymptotic peaks are 1–2° above the intact wedge stability line. Nevertheless, we expect the distribution to become bimodal again after a new frontal thrusting event.

In Style 3, the slope distribution first increases and reaches a peak above the intact wedge stability line. At this point the distribution becomes bimodal with part of the distribution oscillating around the extensionally
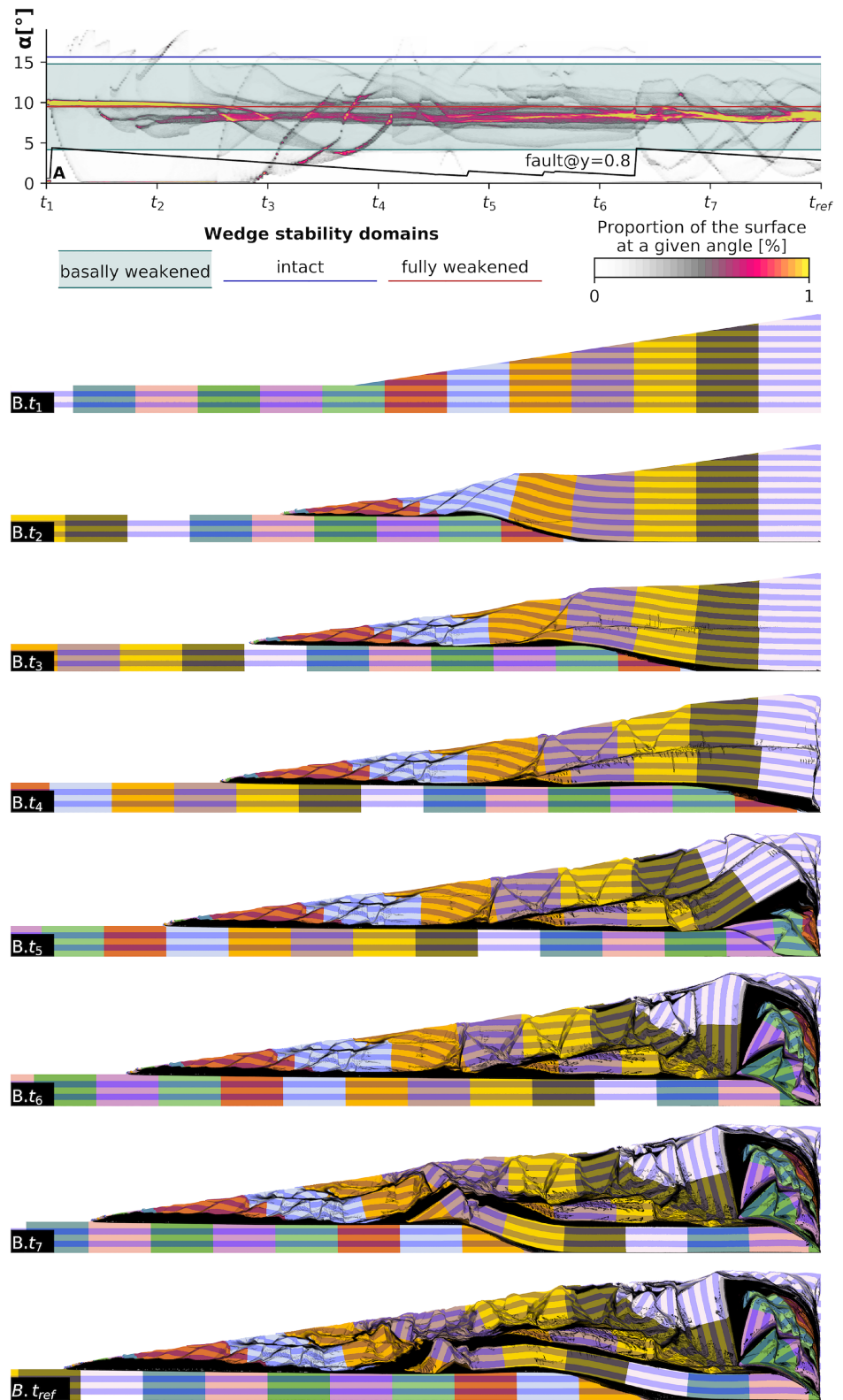
Figure 13. Simulation representative of mechanical mode III ($\lambda = 33\%$, $\chi = 60\%$) with an initial taper. (a) Evolution of the surface angle as a function of time. The colors code for the peak intensity of the surface angle histogram computed for each simulation time step. The theoretical stability range of the basally weakened wedge, intact wedge, and fully weakened wedge are also represented. (b) Wedge geometry (colors) and fault geometry (black). Colors are passive markers of the deformation and are darkened according to plastic strain.

critical state of the basally weakened wedge while another, stronger peak becomes asymptotic toward the fully weakened wedge stability line. Hence, at an advanced stage, because the wedge is intensely faulted, it effectively behaves as if it was completely weakened (see also Figure 10, C.t_{ref}). Faulting events control oscillations of the slope distribution peak close to the extensional state of the weakened wedge, while the asymptotic portion of the distribution is mostly unaffected by faulting events. We interpret that the first peak can reach a value higher than the intact stability line because the base of this small wedge is effectively the lowest thrust which dips at 15° at time t_1 (Figure 10, C.t_1).

3.2.5. Influence of Initial Conditions

In Figure 13 we show the evolution of angles and geometry for a simulation with $\lambda = 33\%$, $\chi = 60\%$, where a wedge with a surface angle of 10° is initially present near the backstop. This initial wedge has a surface angle lower than the stability angle of the intact wedge but higher than the stability angle of a fully weakened wedge (Figure 13a and B.t_1). First, a frontal thrust is created soon after time t_1. The material uplifted along the ramp is extensionally critical (Figure 13a) and therefore deforms by normal thrusting (Figure13, B.t_2). Subsequently, normal thrusts affect domains closer and closer to the backstop and a secondary décollement parallel to the surface forms from time t_3 to t_5. These normal faults reduced the surface angle from 10° initially to 7° where the peak of the surface angle distribution reaches a steady state (Figure 13a). This angle is comparable to the steady-state angle for Style 3 shown in Figure 12c. The ramp reaches the backstop at time t_4, and from t_4 to t_6 the incoming material is deformed in small slices updated along the backstop in a spiral fashion similar to what we observed in Style 3 (Figure 10c). Between time t_6 and t_7 a new basal thrust is created, but the ramp is created below the wedge and doesn't reach the front. The material behind the ramp is then uplifted in a new event of underthrusting. The formation of a long nappe with a fault that ramps up in the middle of the wedge was not observed in our simulation characteristic of Style 3 (Figure 9Gb) but is observed in simulations of mechanical mode II (e.g., Figures 9Fa, 9Ga, and 9Eb). Normal faulting is the dominant mode of deformation in the material that composed the initial taper, while material accreted after the first ramp reached the backstop is deformed in short slices that are exhumed in a spiral pattern typical of Style 3. Long slices also formed in this simulation suggesting that the boundary between mechanical modes II and III occurs for smaller χ or λ compared to the case without initial taper. It seems reasonable to assume that for a higher value of χ, only small slices would form, similar to what is observed in Figure 9.

A movie of the evolution of the geometry and surface angles of this simulation is available in Movie S4.

4. Discussion

4.1. Control of Fault Weakening on Accretionary Prism Dynamics

We demonstrated above the first order control of fault weakening on the structural style for strong-based accretionary prisms. Previous researchers have also investigated the control on fault weakening of the dynamics of accretionary prisms. Such studies showed that fault weakening favors the localization of shear zones, increases the displacement on individual faults, and increases the thickness of thrust sheets (Ellis et al., 2004; Selzer et al., 2007). Willett (1992) investigated the kinematics of a wedge subject to changes in basal friction using numerical methods. In one of his simulations which is initiated with $\phi_b = \phi = 30°$, Willett (1992) describes the formation of a thrust that connects the front of the model to the corner of the box, such that the material is partially underplated. A moderate decrease of basal friction, such that the wedge moves into the stable field, triggers accretion rather than underplating of the material, reducing the surface angle. Then, a further decrease of basal friction triggers the gravitational collapse of the wedge. These three stages of Willett's (1992) simulation correspond to the three mechanical modes described in our present study. However, in Willett (1992), the reduction in basal friction is applied along the lower(basal) boundary, whereas it decreases dynamically along all faults in our models. In contrast to that specific case from Willett (1992), we observe the formation of an antiformal nappe stack (Style 2) and oscillations of the surface slope with cycles of frontal thrust formation and underplating. A further decrease of basal friction (i.e., mode III) in Willett's (1992) case triggers the gravitational collapse of the wedge, which contrasts sharply with our models in which a complete underthrusting of the incoming sediment with exhumation against the back-stop occurs (Style 3). The differences between the two studies outline a fundamental difference between mechanical mode based on the critical taper theory and the structural style which depends on boundary conditions and faulting dynamics.

In another simulation Willett (1992) starts from a situation where $\phi_b < \phi$. The author then applies an increase in basal friction which triggers an increase in surface angles such that the wedge remains
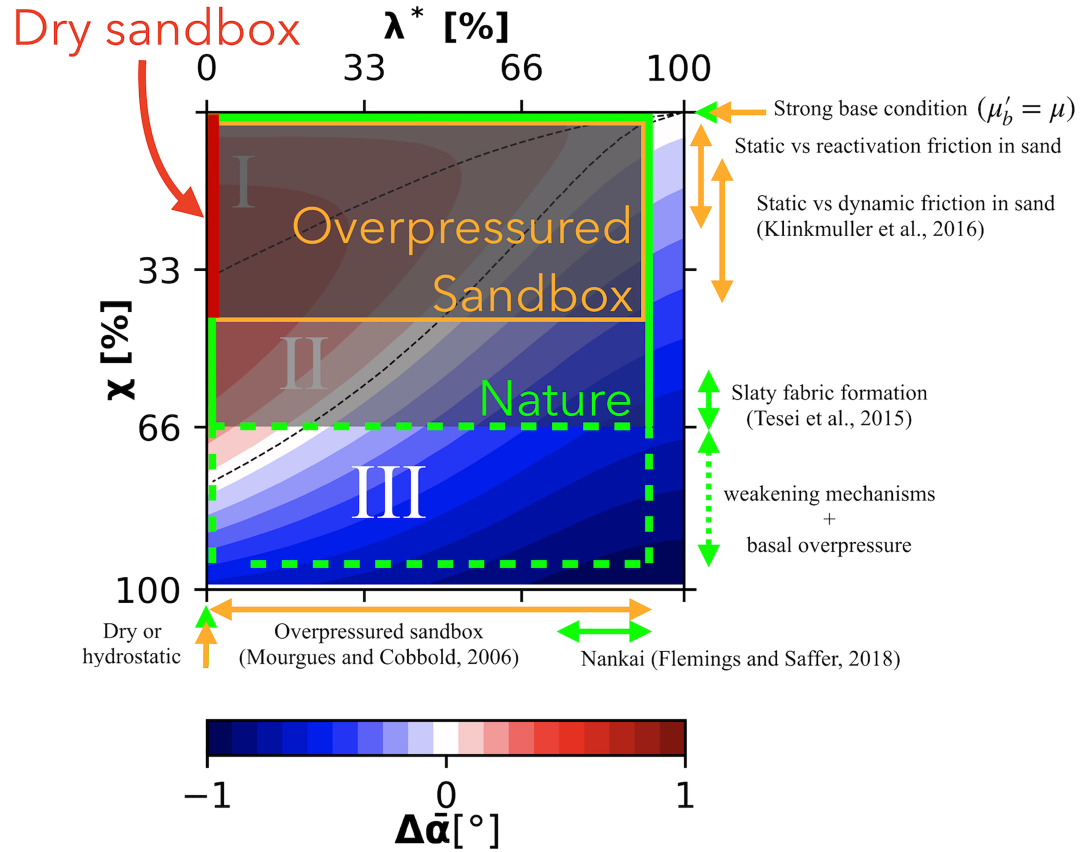
Figure 14. Contour plot of $\Delta\bar{\alpha}$ as a function of the fluid overpressure factor λ^* and the weakening factor χ at $\beta = 0$. Color shaded squares indicate the range of parameters χ and λ^* expected in dry (red) and overpressured (orange) analog sandbox experiments, and in nature (green). All three mechanical modes I, II, and III can be expected in nature. In dry sandbox experiments only mode I and II can be reached, while mode III may be reached in overpressured analog sandbox experiments.

compressively critical. In another study, Ruh et al. (2012) used numerical simulations in which fault weakening was allowed in the wedge but not along its base. As a result, the authors observed an increase in surface angles in response to an effective decrease of the coefficient of friction in the wedge, in agreement with the observations by Willett (1992). The case of an increase in basal friction (ϕ_b) or a decrease in the wedge strength (ϕ), without decreasing the basal strength, is not the purpose of our present study (which we chose to focus on the case $\phi_b = \phi$).

4.2. Comparison With Sandbox Experiments

Analog sandbox experiments have been used extensively to study the dynamics of accretionary prisms (for recent reviews, see Buiter, 2012; Graveleau et al., 2012; Schreurs et al., 2016). Sandbox experiments are often performed in subaerial (dry) conditions, that is, $\lambda^* = 0$, and the sands used in experiments are estimated to have a weakening factor $\chi \approx 2 - 26\%$ if the difference between peak and reactivation friction coefficient is considered, or $\chi \approx 10-44\%$ if instead the difference between peak and dynamic friction coefficient is considered (Klinkmüller et al., 2016) (Figure 14). Therefore, our results predict that sandbox experiments should feature Styles 1 to 2 for $\beta = 0°$. This prediction is in agreement with the observation that sandbox experiments with a strong base ($\phi_b \approx \phi$) are characterized by long thrust sheets and antiformal nappe stacks (e.g., Adam et al., 2005; Del Castello & Cooke, 2007; Gutscher et al., 1996, 1998; Huiqi et al., 1992; Malavieille, 2010). A similar structural style arises in numerical simulations using the discrete element method (Burbidge & Braun, 2002). The model also predicts that Style 3 may be achieved in a sandbox for negative values of β. Sandbox models typically do not show the kind of domino deformation displayed in our models when $\lambda^* = 0\%$ (Figure 9), but more closely resembles the style of simulations that we obtain for $\lambda^* = 33\%$. These differences may have a few main causes. First, in analog experiments the basal friction is never as high as the internal friction. Second, sand can compact and dilate whereas in our model is incompressible

with nonassociated plasticity (i.e., the dilation angle is zero). Finally, the weakening algorithm we employ is a simplification of the strain weakening that applies to sand.

Some researchers have investigated the control of fluid pressure in analog sandbox experiments using compressed air flow (Cobbold & Castro, 1999; Cobbold et al., 2001; Mourgues & Cobbold, 2006). Values of λ^* as high as 0.8–0.9 can be reached (Mourgues & Cobbold, 2006; Pons & Mourgues, 2012). Therefore, it seems theoretically possible to reproduce the results of this study with an analog apparatus (Figure 14). However, to the knowledge of the authors, experiment with an initially strong base, and high fluid pressure that could generate Style 3 have not been performed yet.

4.3. λ^* and χ in Nature

The pore fluid pressure factor λ and pore fluid overpressure factor λ^* have been estimated in natural accretionary prism using a variety of methods. A review of those methods and results is given by Saffer and Tobin (2011). Generally the fluid overpressure in accretionary prisms is relatively high. Borehole-based studies indicate that within 1–4 km of the trench, $\lambda^* = 0.20 - 0.91$ within underthrusting sediment. Recently, Flemings and Saffer (2018) have estimated the fluid pressure in the Nankai accretionary prism from porosity measurements with a critical state soil model. They determined that $\lambda^* = 0.7 - 0.9$ for a range of assumed friction angles between 5° and 30° (Figure 14).

The weakening factor χ can be associated with several mechanisms in nature. First, highly reflective décollements in seismic reflection data are often interpreted as resulting from elevated pore fluid pressure localized on the décollement (Bangs et al., 2009; Park et al., 2002, 2010; Ranero et al., 2008). For instance, Tobin et al. (1994) estimated that $\lambda^* = 0.86 - 0.98$ along the frontal thrust of the central Oregon margin, based on seismic reflection waveform, amplitude modeling, and laboratory measurements on core samples. In rocks rich in both carbonate and clay minerals, the departure of calcite during the early stages of faulting play an important role in the early weakening of faults (Lacroix et al., 2015). This weakening mechanism is associated with the development of a slaty fabric. Tesei et al. (2015) measured the friction coefficient of fault material from clay-rich sediment. They measured friction coefficients $\mu = 0.17 - 0.26$ in fault rocks showing a slaty cleavage, whereas powders made of the same material and representative of the material without fabric had $\mu = 0.49 - 0.55$. The strength reduction due to fabric formation correspond to $\chi = 60 - 65\%$ (Figure 14). Other mechanisms include the formation of clay gouge and the associated dynamic metamorphism that triggers the transformation of illite into smectite (Reches & Dewers, 2005; Vrolijk & van der Pluijm, 1999), the process of dynamic weakening during earthquakes (Burridge & Knopoff, 1967; Dieterich, 1979; Di Toro et al., 2011; Ruina, 1983), or the decrease of effective stress due to the shearing or thinning of a shear zone (Le Pourhiet, 2013; Scott et al., 1994).

These estimates of χ and λ^* from natural examples indicate that mechanical mode III is likely to be reached in nature. However, whether mechanical mode III would be expressed as structural Style 3 is not clear and would depend on boundary conditions. The spiral pattern characteristic of Style 3 is not observed in nature as far as the author knows. In nature mechanical mode III deformation of the backstop may allow all the material to be subducted instead of forming the spiral pattern characteristic of Style 3. Further study is necessary to test this hypothesis.

4.4. Applicability to Natural Structures
4.4.1. Nappe Stacking

Antiformal nappe stacks are essential structures in fold-and-thrust belts and accretionary prisms. Examples are the Helvetic nappes in Switzerland (Escher et al., 1993) or the Alberta foothills in Canada (Fermor & Moffat, 1992). The base of tectonic nappes is often composed of mechanically weaker horizons. In this case, the applicability of our model is limited, and models incorporating several weak layers are more appropriate to reproduce these structural styles (Massoli et al., 2006; Ruh et al., 2012). On the other hand, the mechanism of dynamical weakening described in our study can explain nappe stacks where no particularly weak horizons are present, such as in the accretionary prism of the Aleutian Trench (Gutscher et al., 1998). Our results suggest that in these conditions the formation of an antiformal nappe stack is restricted to mechanical conditions that are close to the transition between modes I and II.

4.4.2. Slope Aprons and Olistostrome

In our numerical models we observe shallow gravity instabilities /similar to slope aprons/ for simulations in mechanical modes II and III. This result is consistent with the prediction of Mourgues et al. (2014). In their analysis, they use the concept of the safety factor ($FS = \tan(\alpha) / \tan(\alpha_{max})$) often used in engineering and

which varies very similarly to $\bar{\alpha}$. When those numbers are close to 1, shallow gravity sliding occurs. When FS or $\bar{\alpha}$ decreases, Mourgues et al. (2014) suggest that deep normal faults reaching the décollement are expected. This theoretical prediction is consistent with the transition that we observe from shallow gravity sliding in Style 2 to deep normal faulting in Style 3.

Style 3 could explain the formation of olistostromes and submarine landslides. A complementary question in this regard is whether extensional faults are mostly planar in the third direction, or whether they are curved and thus define lentils as is commonly observed for gravitational instabilities. In our model, we neglected inertia and employed a certain cohesion to limit the minimum strength of rocks near the surface. Without this limitation, gravitational instabilities would rapidly run down the surface slope. It would thus form submarine landslides.

4.4.3. Erosive Margins/Subduction Channel

Subduction channels have been imaged, for example, in Chile, Costa Rica, Nicaragua, or Ecuador (Ranero et al., 2008; Sage et al., 2006; von Huene & Ranero, 2003). Several authors have proposed a sandbox configuration that models the development of basal erosion and the formation of a subduction channel. It consists of a preexisting initial wedge and an incoming horizontal sediment layer. An outflow is allowed through a "subduction gate" located below the backstop (Albert et al., 2018; Gutscher et al., 1996, 1998; Kukowski & Oncken, 2006). These studies showed that in high-basal-friction conditions, a subduction channel forms spontaneously (Gutscher et al., 1998; Kukowski & Oncken, 2006). The shape can vary as a function of the outflow (Albert et al., 2018). These experiments suggest that given appropriate initial and boundary conditions, the mechanical modes I and II result in the formation of a subduction channel rather than the antiformal stack characteristic of Style 2. Our results suggest that a subduction channel also tends to form spontaneously in mechanical mode III, although this hypothesis remains to be validated, for example, by performing simulations with the initial and boundary conditions cited above.

4.5. A General Mechanism for Style 3

The mechanical behavior of mechanical mode III is mostly controlled by the fact that the surface angle is such that the upper wedge is critically neutral, but the incoming material is always in the undercritical regime. The wedge needs to reach the critical taper to overcome basal shear stress and initiate displacement along the base. Since the regime is undercritical in the incoming sediment, this condition is never met, and the material is instead underthrusted below the weak wedge. The material only deforms against the backstop because there, the stress field is forced to reach the yield state. Once the material reaches the backstop, it can only go up and is therefore exhumed. In our model, the taper remains undercritical because of pervasive deformation and fault weakening. Surface processes, that is, erosion and sedimentation, can also control the slope so that the taper remains undercritical (Willett, 1999). Therefore, surface processes can also favor deformation at the back/rear rather than at the front (Simpson, 2010) and trigger exhumation (Burbank, 2002; Dahlen & Suppe, 1988; Malavieille & Konstantinovskaya, 2010; Mary et al., 2013).

4.6. Limits of the Method

Many processes in nature can cause weakening of faults. We did not model the physics of these processes, but instead we used a standard parameterization of strain softening that links plastic strain to a weakening factor (equation (25)). This numerical scheme is often used but has the important caveat of being mesh-sensitive. In this study, all simulations have been performed at the same resolution such that simulations are consistent with each other. Furthermore, we performed a test to assess the sensitivity of the structural style on the numerical resolution (Figure 15). We ran the characteristic simulations of Styles 2 and 3 at resolution of $H/16, H/32, H/64$ (i.e., default), and $H/128$. The test reveals that resolution has some impact on the location and angle of faults as shown in Kaus (2010). At the lowest resolution ($H/16$) it seems that the structural style changes through time. However, this artefact disappears at higher resolution. For resolution greater than $H/32$ the resolution does not influence the characteristics of the structural style such as the surface angle, shallow surface instabilities, gravitational collapse, underthrusting, exhumation, or antiformal nappe stacking. The simulation with an initial taper outlines the fact initial conditions affect the structural style, even though the overall kinematics remains similar to a case without initial taper. Furthermore, testing the control of backstop deformation on the structual style is out of the scope of this study, but it is without a doubt an important factor and may allow the incoming material to be completely underthrusted instead of being accreted at the base of the prism in a spiral pattern as it is the case here.
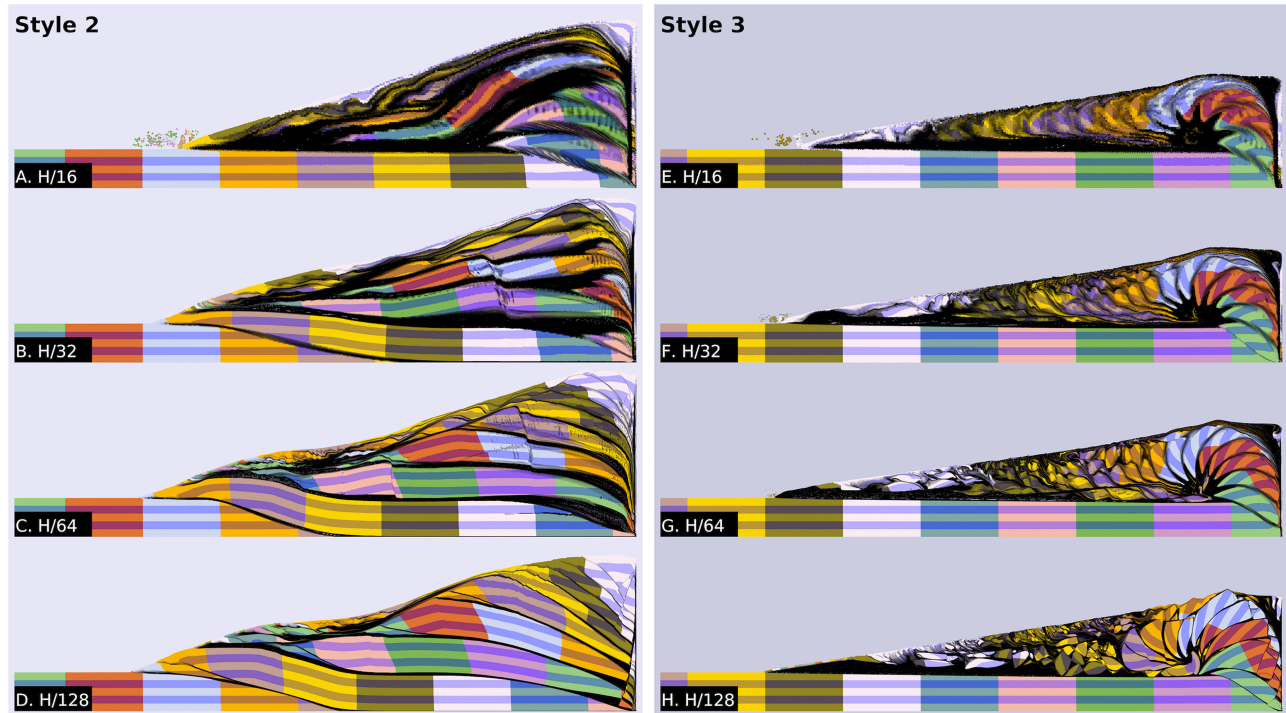
Figure 15. Test of the sensitivity of numerical resolution on the structural. At all the resolutions tested the same characteristics of the strucural style are observed. (a–d) Simulations of the wedge characteristic of Style 2 ($\chi = 20\%$, $\lambda^* = 33\%$) at resolutions of $H/16$ (a), $H/32$ (b), $H/64$ (c), and $H/128$ (d). (e–h) Simulations of the wedge characteristic of Style 3 ($\chi = 20\%$, $\lambda^* = 33\%$) at resolutions of $H/16$ (e), $H/32$ (f), $H/64$ (g), and $H/128$ (h).

In natural accretionary prisms fluid pressure is heterogeneous and is affected by permeability and tectonic stresses. In the theoretical model it is assumed that $\lambda_b^* = \lambda^*$ and that the fluid pressure varies proportionally to the σ_z, that is, the normal stress in the direction perpendicular to β. Thus, a constant λ means that the pore pressure increases linearly in the z direction.

In our numerical model we assume instead that the fluid pressure is proportional to the pressure P. Therefore, a constant value of λ means that the fluid pressure is sensitive to deviatoric stresses as well. This assumption allows a simple definition of the yield stress. Either assumption is arbitrary since it does not take into account the physics of fluid flow in a porous medium (e.g., Keller et al., 2013). We have demonstrated that the range of surface angles in the model is bounded by theoretical predictions (Figure 12). Therefore, the difference in the definition of λ does not hinder the comparison. However, specific structural features such as the onset of surface tectonics could appear for slightly different combinations of λ^* and χ. We can also note that the solution of Dahlen (1984) makes use of a small angle approximation in the definition of λ which has a significant consequence for surface angles (Wang et al., 2006). Mourgues et al. (2014) show a comparison between solutions with and without the small angle approximation (their Figure 4) which outlines that the transition between modes I and II can be shifted by a few percents in χ or λ^*.

5. Conclusion

In nature, underthrusting is often associated with weak basal faults, although static mechanical analysis (critical taper theory) predicts that weak basal faults promote accretion while strong basal faults promote underthrusting. We performed mathematical analyses and numerical simulations to determine whether permanent fault weakening promotes or inhibits underthrusting. First, we used the critical taper theory to identify mechanical modes triggered by the transition from an intact state where the basal friction is as strong as the intact sediment ($\mu_b^* = \mu^*$) to a second state with weak internal and/or basal faults. Second, we performed numerical simulations of the deformation of an initally flat layer of plastic (brittle) material submitted to sandbox-like boundary conditions. Fault weakening was applied to yielded areas using strain softening. The numerical results are consistent with the analytical solution in terms of surface angles and show that given the chosen initial and boundary condtions the mechanical modes are expressed as

a continuum of structural styles, with three archetypal styles at the boundaries between mechanical modes. In Style 1, the wedge is composed of thin tectonic slices oblique to the base. Style 2 is characterized by the formation of an antiformal stack composed of tectonic nappes as thick as the incoming material. Finally, Style 3 is characterized by full underplating of the incoming material under a weak upper prism formed by exhumed material that then undergoes gravity collapse. The transition from Styles 1 to 3 can be triggered by an increase of pore fluid pressure in the wedge and/or by a decrease of fault strength relative to the intact material. Our results predict that Styles 1 and 2 are likely to occur in subaerial sandbox experiments for positive basal slopes ($\beta > 0$), whereas Style 3 can only occur for negative basal slopes ($\beta \leq 0$). On the other hand rock experiments and fluid pressure estimates from the literature suggest that all three mechanical modes are likely to occur in nature for positive basal slopes. The conditions to realize mechanical mode III in the laboratory may be attained if using a sandbox apparatus allowing for high overpressure in the wedge. We conclude that in the condition that the base of the wedge is initially strong, permanent fault weakening promotes underthrusting. Thus, this contribution enlightens the control of the dynamic evolution of material properties on the formation of subduction channels, slope instabilities, and antiformal nappe stacks. In future works the model can be refined to further assess the its validity and explore new structural styles. Modifications likely to have first order implications include a weakening law based on fundamental principles and boundary conditions that allow material to go beyond the accretionary prism region.

Appendix A: Numerical Methods

A1. Governing Equations

The mathematical model is based on the Stokes equations that describe the momentum (A1) and mass conservation (A2) of a continuum in the case where inertia forces are negligible (i.e., the Reynolds number $Re \approx 0$). Here the continuum is assumed to be incompressible.

$$\frac{\partial \tau_{ij}}{\partial x_j} - \frac{\partial P}{\partial x_i} + \rho g_i = 0, \tag{A1}$$

$$\frac{\partial v_i}{\partial x_i} = 0, \tag{A2}$$

where x_i are the spatial coordinates, τ_{ij} are the components of the deviatoric stress tensor, v_i are the components of the velocity vector, ρ is the density, and g_i are the components of the acceleration of gravity vector. We use the convention that pressure P is positive under compression; thus, $P = -1/3\tau_{ii}$. We use Einstein's summation convention. The relation between the velocity vector field and the strain tensor field is described by constitutive equations.

A2. Constitutive Equations

Let us define the deviatoric strain rate tensor:

$$\dot{\epsilon}_{ij} = \frac{1}{2}(\frac{\partial v_i}{\partial x_j} + \frac{\partial v_j}{\partial x_i}) - \frac{1}{3}\delta_{ij}\frac{\partial v_i}{\partial x_i}, \tag{A3}$$

where δ_{ij} is the Kronecker delta. We also define the notation

$$X_{II} = \sqrt{\frac{1}{4}(X_{11} - X_{22})^2 + X_{12} * X_{21}}, \tag{A4}$$

where X_{II} is the square root of the second invariant of a generic tensor X.

We assume a Maxwell body with visco-elasto-plastic rheology. Thus, the strain rate is decomposed additively.

$$\dot{\epsilon}_{ij} = \dot{\epsilon}_{ij}^v + \dot{\epsilon}_{ij}^e + \dot{\epsilon}_{ij}^p, \tag{A5}$$

where superscripts v, e, and p denote the viscous, elastic, and plastic parts of the total deviatoric strain rate tensor, respectively. The deviatoric strain rate tensor and the deviatoric stress tensor are linked by the following constitutive relationships

$$\dot{\epsilon}_{ij}^v = \frac{1}{2\eta}\tau_{ij}, \tag{A6}$$

$$\dot{\epsilon}^e_{ij} = \frac{1}{2G}\frac{\check{D}\tau_{ij}}{Dt} \approx \frac{1}{2G}\frac{\tau_{ij}{}^{new} - \tau_{ij}O}{\Delta t}, \tag{A7}$$

and

$$\begin{cases} \dot{\epsilon}^p_{ij} = 0, & \text{when} \quad F < 0, \\ \dot{\epsilon}^p_{ij} = \frac{\kappa}{2}\frac{\tau_{ij}}{\tau_{II}}, & \text{when} \quad F = 0, \end{cases} \tag{A8}$$

where η is the viscosity, G is the elastic shear modulus, and κ is the plastic multiplier. $\check{D}\tau_{ij}/Dt$ is the objective co-rotational time derivative of the deviatoric stress tensor which we approximate using a first order finite difference in time where Δt is small increment of time, and $\tau_{ij}{}^{old}$ and $\tau_{ij}{}^{new}$ are the components of the deviatoric stress tensor at time t and $t + \Delta t$, respectively. Equation (A8) prescribes the plastic flow rule with the yield function

$$F = \tau_{II} - (1 - \chi w(\epsilon_p))\tau_y, \tag{A9}$$

with

$$\tau_y = C cos(\phi) + (1 - \lambda)P sin(\phi)), \tag{A10}$$

where τ_y is the Mohr-Coulomb yield stress, C is the cohesion, and ϕ is the friction angle. χ is a weakening parameter, and $w(\epsilon_p)$ is a weighting piecewise linear function of the plastic strain ϵ_p defined as

$$\begin{cases} w(\epsilon_p) & = 0, \quad \text{when } \epsilon_p <= \epsilon_{pws}, \\ w(\epsilon_p) & = \frac{\epsilon_p - \epsilon_{pws}}{\epsilon_{pwe} - \epsilon_{pws}}, \quad \text{when } \epsilon_p ws < \epsilon_{psilon_p} <= \epsilon_{pwe}, \\ w(\epsilon_{psilon_p}) & = 1, \quad \text{when } \epsilon_p > \epsilon_{pwe}, \end{cases} \tag{A11}$$

where $\epsilon_p ws$ and $\epsilon_p we$ are the plastic strain values at which the weakening parameter starts and finishes to increase, respectively. The plastic strain is defined as

$$\epsilon_{psilon_p} = \int_0^t \dot{\epsilon}^p_{II} dt. \tag{A12}$$

A3. Final Formulation of Stress

So far we have defined the stress tensor as a function of the independent parts of the deviatoric strain rate tensor $\dot{\epsilon}^v_{ij}$, $\dot{\epsilon}^e_{ij}$, and $\dot{\epsilon}^p_{ij}$. Within the numerical scheme, it is convenient to get a new expression of the stress as a function of the total deviatoric strain rate tensor and the deviatoric stress tensor at a previous time step. Solving (A6) for τ_{ij} and substituting (A5) yield

$$\tau_{ij} = 2\eta(\dot{\epsilon}_{ij} - \dot{\epsilon}^e_{ij} - \dot{\epsilon}^p_{ij}). \tag{A13}$$

Substituting (A7) in (A13) yields

$$\tau_{ij} = 2\eta(\dot{\epsilon}_{ij} - \frac{\tau_{ij} - \tau_{ij}{}^{old}}{2G\Delta t} - \dot{\epsilon}^p_{ij}). \tag{A14}$$

(A14) can be rewritten as

$$\tau_{ij} = 2\eta^{ve}(\dot{\epsilon}^{ve}_{ij} - \dot{\epsilon}^p_{ij}), \tag{A15}$$

where η^{ve} and $\dot{\epsilon}^{ve}_{ij}$ are an effective visco-elastic viscosity and an effective visco-elastic strain rate, respectively, such that

$$\eta^{ve} = \frac{1}{\frac{1}{\eta} + \frac{1}{G\Delta t}}, \tag{A16}$$

$$\dot{\epsilon}^{ve}_{ij} = \dot{\epsilon}_{ij} + \frac{\tau^{old}_{ij}}{2G\Delta t}. \tag{A17}$$

We can also define an effective visco-elastic stress $\tau_{ij}{}^{ve} = 2\eta^{ve}\epsilon^{ve}_{ij}$. (A8) can be rewritten as

$$\dot{\epsilon}_{ij}{}^p = \frac{\kappa}{2} \frac{\tau_{ij}{}^{ve}}{\tau_{II}{}^{ve}} = \frac{\kappa}{2} \frac{\dot{\epsilon}_{ij}^{ve}}{\dot{\epsilon}_{II}^{ve}}. \tag{A18}$$

Substituting (A18) in (A15) yields

$$\tau_{ij} = 2\eta^{ve}\dot{\epsilon}_{ij}^{ve}\Lambda, \tag{A19}$$

with

$$\Lambda = 1 - \frac{\kappa}{2\dot{\epsilon}_{II}^{ve}}. \tag{A20}$$

The yield condition is satisfied if

$$\Lambda = \frac{(1-\chi)\tau_y}{\tau_{II}{}^{ve}}, \quad \text{when} \quad F = 0. \tag{A21}$$

A4. Numerical Scheme

The numerical scheme is based on the finite-difference marker-in-cell method (Harlow and Welch, 1965; Gerya and Yuen, 2003). All invariants are computed on a staggered grid. The system of equations is solved for v_x, v_y, and P using the implicit direct solver PARDISO v6.0.0 (De Coninck et al., 2016; Kourounis et al., 2018; Verbosio et al., 2017). We compute the yield function directly on the grid, and markers are used only to advect material and physical properties. At the end of a time step the components of the stress tensor are interpolated from the grid to the markers. Then, we apply the rotation to the stress field and advect the markers. Finally, stress components are advected back from the markers to the grid.

Appendix B: Critical Taper Script

```
#!/usr/bin/env python3
# -*- coding: utf-8 -*-
"""
This script constructs the critical taper envelope (CTE) using the
analytical solution of Lehner (1986).The nomenclature of angles follows
Lehner (1986). The solution has been benchmarked against the graphical
method of Dahlen (1984). If you use this function please cite this
repository and the original paper:
1. Dahlen, F. A. (1984). Noncohesive critical Coulomb wedges: An exact
solution. Journal of Geophysical Research: Solid Earth, 89(B12):
10125-10133.
2. Lehner, F. K. (1986). Comments on "Noncohesive critical Coulomb wedges:
an exact solution'' by F. A Dahlen. Journal of Geophysical Research,
91(B1):793-796
3. this paper
4. Arthur Bauville. (2019, June 21). abauville/CriticalTaper-utils 1.0.1
(Version 1.0.1). Zenodo. http://doi.org/10.5281/zenodo.3251524
"""

# Libraries
# =============================================
import numpy as np
import matplotlib.pyplot as plt
from numpy import sin, tan, pi, arcsin, arctan

# Units
# =============================================
deg = pi/180.0          # degrees (in radians)
kg = 1.0                # kilogram
m = 1.0                 # m
```

```
# Basic quantities
# ===============================================
rho_w           = 1,000.0 * kg/m**3 # water density
rho             = 2,500.0 * kg/m**3 # wedge density

phi             = 30.0 * deg        # wedge friction angle
phi_b           = 10.0 * deg        # base friction angle

Lambda          = 0.6              # wedge fluid pressure factor
Lambda_b        = 0.9              # base fluid pressure factor

# Derivative quantities
# ===============================================
Lambda_hydro = rho_w/rho                              # hydrostatic fluid
                                                       pressure factor
Lambda_ov    = 1.0 - (1.0-Lambda )/(1.0-Lambda_hydro) # wedge fluid
                                                       overpressure factor
Lambda_b_ov  = 1.0 - (1.0-Lambda_b)/(1.0-Lambda_hydro) # base fluid
                                                       overpressure factor

mu           = tan(phi)                              # wedge friction coeff.
mu_b         = tan(phi_b)                            # base friction coeff.
phi_b_p      = arctan(mu_b*(1.0-Lambda_b)/(1.0-Lambda))# base effective
                                                       friction angle

alpha_m      = arctan((1.0-Lambda_b_ov)*mu_b)        # Left corner of the CTE
alpha_max    = arctan((1.0-Lambda_ov)*mu)            # Angle of repose

# Solution vectors
# ===============================================
n = 1,000 # number of points per segment
nSeg = 4 # number of segment
alpha_all = np.zeros(nSeg*n) # surface angles of all segments
beta_all = np.zeros(nSeg*n) # basal angles of all segments
# List containing the alpha values at beginning and end of segments
alpha_list = [alpha_m,alpha_max,-alpha_m,-alpha_max,alpha_m]

# Compute beta as a function of alpha
# ===============================================
for i in range(nSeg): # Loop through the 4 segments
 alpha = np.linspace(alpha_list[i],alpha_list[i+1],n)# surface angle
 alpha_p = arctan( 1.0/(1.0-Lambda_ov)*tan(alpha) )  # effective surface
                                                       angle

 theta = arcsin(sin(phi_b_p)/sin(phi))               # auxiliary friction angle
 gamma = arcsin(sin(alpha_p)/sin(phi))               # auxiliary surface angle

 if i%2==0: psi_0 = 0.5*(-gamma - alpha_p + pi)      # psi_0 = psi_0_a
 else: psi_0 = 0.5*(+gamma - alpha_p)                # psi_0 = psi_0_p


 if i<2: psi_b = 0.5*(-theta - phi_b_p + pi)         # psi_0 = pi/2-psi_b_1
 else: psi_b = 0.5*(+theta - phi_b_p)                # psi_0 = psi_b_3

 beta = psi_b-psi_0-alpha
 beta[beta<-pi/4.0] += pi
```

```
 beta_all[i*n:(i+1)*n] = beta
 alpha_all[i*n:(i+1)*n] = alpha
# end of segment loop

# Plotting
# ===========================================
plt.figure(1)
plt.clf()
plt.fill(beta_all/deg,alpha_all/deg)
plt.xlabel('$\\beta [^\\circ]$')
plt.ylabel('$\\alpha [^\\circ]$')
```

References

Adam, J., Urai, J. L., Wieneke, B., Oncken, O., Pfeiffer, K., Kukowski, N., et al. (2005). Shear localisation and strain distribution during tectonic faulting—New insights from granular-flow experiments and high-resolution optical image correlation techniques. *Journal of Structural Geology*, *27*(2), 299–301.

Albert, F., Kukowski, N., Tassara, A., & Oncken, O. (2018). Material transfer and subduction channel segmentation at erosive continental margins: Insights from scaled analogue experiments. *Tectonophysics*, *749*, 46–61.

Bangs, N. L. B., Moore, G. F., Gulick, S. P. S., Pangborn, E. M., Tobin, H. J., Kuramoto, S., & Taira, A. (2009). Broad, weak regions of the Nankai Megathrust and implications for shallow coseismic slip. *Earth and Planetary Science Letters*, *284*(1-2), 44–49.

Bauville, A. (2019). CriticalTaper-utils. https://zenodo.org/record/2646743#.XLlGNOszbUI

Buiter, S. J. H. (2012). A review of brittle compressional wedge models. *Tectonophysics*, *530-531*(0040), 1–17.

Buiter, S. J. H., Babeyko, A. Y., Ellis, S., Gerya, T. V., Kaus, BorisJ. P., Kellner, A., et al. (2006). The numerical sandbox: Comparison of model results for a shortening and an extension experiment. *Geological Society, London, Special Publications*, *253*(1), 29–64.

Buiter, S. J. H., Schreurs, G., Albertz, M., Gerya, T. V., Kaus, B., Landry, W., et al. (2016). Benchmarking numerical models of brittle thrust wedges. *Journal of Structural Geology*, *92*, 140–177.

Burbank, D. W. (2002). Rates of erosion and their implications for exhumation. *Mineralogical Magazine*, *66*(01), 25–52.

Burbidge, D. R., & Braun, J. (2002). Numerical models of the evolution of accretionary wedges and fold-and-thrust belts using the distinct-element method. *Geophysical Journal International*, *148*(3), 542–561.

Burridge, R., & Knopoff, L. (1967). Model and theoretical seismicity. *Bulletin of the Seismological Society of America*, *57*(3), 341–371.

Chapple, W. M. (1978). Mechanics of thin-skinned fold-and-thrust belts. *Geological Society of America Bulletin*, *89*(8), 1189.

Clift, P., & Vannuchi, P. (2004). Controls on tectonic accretion versus erosion in subduction zones: Implications for the origin and recycling of the continental crust. *Reviews of Geophysics*, *42*, RG2001. https://doi.org/10.1029/2003RG000127

Cloos, M., & Shreve, R. L. (1988a). Subduction-channel model of prism accretion, melange formation, sediment subduction, and subduction erosion at convergent plate margins: 1. Background and description. *Pure and Applied Geophysics PAGEOPH*, *128*(3-4), 455–500.

Cloos, M., & Shreve, R. L. (1988b). Subduction-channel model of prism accretion, melange formation, sediment subduction, and subduction erosion at convergent plate margins: 2. Implications and discussion. *Pure and Applied Geophysics PAGEOPH*, *128*(3-4), 501–545.

Cobbold, P. R, & Castro, L (1999). Fluid pressure and effective stress in sandbox models. *Tectonophysics*, *301*(1-2), 1–19.

Cobbold, P. R., Durand, S., & Mourgues, R. (2001). Sandbox modelling of thrust wedges with fluid-assisted detachments. *Tectonophysics*, *334*(3-4), 245–258.

Crameri, F., Schmeling, H., Golabek, G. J., Duretz, T., Orendt, R., Buiter, S. J. H., et al. (2012). A comparison of numerical surface topography calculations in geodynamic modelling: An evaluation of the 'sticky air' method. *Geophysical Journal International*, *189*(1), 38–54.

Cubas, N., Avouac, J. P., Leroy, Y. M., & Pons, A. (2013). Low friction along the high slip patch of the 2011 Mw 9.0 Tohoku-oki earthquake required from the wedge structure and extensional splay faults. *Geophysical Research Letters*, *40*, 4231–4237. https://doi.org/10.1002/grl.50682

Dahlen, F. A. (1984). Noncohesive critical Coulomb wedges: An exact solution. *Journal of Geophysical Research*, *89*(B12), 10,125–10,133. https://doi.org/10.1029/JB089iB12p10125

Dahlen, F. A., & Suppe, J. (1988). Mechanics, growth, and erosion of mountain belts. *Processes in Continental Lithospheric Deformation: Geological Society of America Special Paper*, *218*, 161–178.

Dahlen, F. A., Suppe, J., & Davis, D. (1983). Mechanics of fold-and-thrust belts and accretionary wedges cohesive Coulomb theory. *Journal of Geophysical Research*, *88*(B2), 1153–1172.

Davis, D., Suppe, J., & Dahlen, F. A. (1983). Mechanics of fold-and-thrust belts and accretionary wedges. *Journal of Geophysical Research*, *88*(B2), 1153–1172. https://doi.org/10.1029/JB088iB02p01153

De Coninck, A., De Baets, B., Kourounis, D., Verbosio, F., Schenk, O., Maenhout, S., & Fostier, J. (2016). Needles: Toward large-scale genomic prediction with marker-by-environment interaction. *Genetics*, *203*(1), 543–555. https://doi.org/10.1534/genetics.115.179887

Del Castello, M., & Cooke, M. L. (2007). Underthrusting-accretion cycle: Work budget as revealed by the boundary element method. *Journal of Geophysical Research*, *112*, B12404. https://doi.org/10.1029/2007JB004997

Di Toro, G., Han, R., Hirose, T., De Paola, N., Nielsen, S., Mizoguchi, K., et al. (2011). Fault lubrication during earthquakes. *Nature*, *471*(7339), 494–498.

Dieterich, J. H. (1979). Modeling of rock friction: 1. Experimental results and constitutive equations. *Journal of Geophysical Research*, *84*(B5), 2161–2168. https://doi.org/10.1029/JB084iB05p02161

Ellis, S., Schreurs, G., & Panien, M. (2004). Comparisons between analogue and numerical models of thrust wedge development. *Journal of Structural Geology*, *26*(9), 1659–1675.

Escher, A., Masson, H., & Steck, A. (1993). Nappe geometry in the Western Swiss Alps. *Journal of Structural Geology*, *15*(3-5), 501–509.

Fermor, P. R., & Moffat (1992). Tectonics and structure of the Western Canada Foreland Basin: Chapter 3. M 55: Foreland basins and fold belts, (pp. 81–105) AAPG Special Volumes.

Flemings, P. B., & Saffer, D. M. (2018). Pressure and stress prediction in the Nankai accretionary prism: A critical state soil mechanics porosity-based approach. *Journal of Geophysical Research: Solid Earth*, *123*, 1089–1115. https://doi.org/10.1002/2017JB015025

Gao, X., & Wang, K. (2014). Strength of stick-slip and creeping subduction megathrusts from heat flow observations. *Science (New York, N.Y.)*, *345*(6200), 1038–41.

Gerya, T. B., & Yuen, D. A. (2003). Characteristics-based marker-in-cell method with conservative finite-differences schemes for modeling geological flows with strongly variable transport properties. *Physics of the Earth and Planetary Interiors*, *140*, 295–320.

Graveleau, F., Malavieille, J., & Dominguez, S. (2012). Experimental modelling of orogenic wedges: A review. *Tectonophysics*, *538-540*, 1–66.

Gutscher, M. A., Kukowski, N., Malavieille, J., & Lallemand, S. (1996). Cyclical behavior of thrust wedges: Insights from high basal friction sandbox experiments. *Geology*, *24*(2), 135–138.

Gutscher, M. A., Kukowski, N., Malavieille, J., & Lallemand, S. (1998). Material transfer in accretionary wedges from analysis of a systematic series of analog experiments. *Journal of Structural Geology*, *20*(4), 407–416.

Harlow, F. H., & Welch, J. E. (1965). Numerical calculation of time-dependent viscous incompressible flow of fluid with free surface. *Physics of Fluids*, *8*, 2182.

Hubbert, M. K., & Rubey, W. W. (1959). Role of fluid pressure in mechanics of overthrust faulting I. Mechancis of fluid-filled porous solids and its application to overthrust faulting. *GSA Bulletin*, *70*(2), 115–166.

Huiqi, L., McClay, K. R., & Powell, D. (1992). Physical models of thrust wedges. In K. R. McClay (Ed.), *Physical models of thrust wedges, thrust tectonics* (pp. 71–81). Dordrecht: Springer. https://doi.org/10.1007/978-94-011-3066-0_6

Kaus, B. J. P. (2010). Factors that control the angle of shear bands in geodynamic numerical models of brittle deformation. *Tectonophysics*, *484*(1-4), 36–47.

Keller, T., May, D. A., & Kaus, B. J. P. (2013). Numerical modelling of magma dynamics coupled to tectonic deformation of lithosphere and crust. *Geophysical Journal International*, *195*(3), 1406–1442.

Klinkmüller, M., Schreurs, G., Rosenau, M., & Kemnitz, H. (2016). Properties of granular analogue model materials: A community wide survey. *Tectonophysics*, *684*, 23–38.

Kodaira, S., Nakamura, Y., Yamamoto, Y., Obana, K., Fujie, G., No, T., et al. (2017). Depth-varying structural characters in the rupture zone of the 2011 Tohoku-oki earthquake. *Geosphere*, *13*(5), 1408–1424.

Kourounis, D., Fuchs, A., & Schenk, O. (2018). Towards the next generation of multiperiod optimal power flow solvers. *IEEE Transactions on Power Systems*, *PP*(99), 1–10. https://doi.org/10.1109/TPWRS.2017.2789187

Kukowski, N., & Oncken, O. (2006). Subduction erosion—The "normal" mode of fore-arc material transfer along the Chilean margin? In O. Oncken (Ed.), *The Andes: Active subduction orogeny* (pp. 217–236). Berlin, Heidelberg: Springer.

Lacroix, B., Tesei, T., Oliot, E., Lahfid, A., & Collettini, C. (2015). Early weakening processes inside thrust fault. *Tectonics*, *34*, 1396–1411. https://doi.org/10.1002/2014TC003716

Lallemand, S. (1995). High rates of arc consumption by subduction processes: Some consequences. *Geology*, *23*(6), 551.

Le Pourhiet, L. (2013). Strain localization due to structural softening during pressure sensitive rate independent yielding. *Bulletin de la Societe Geologique de France*, *184*(4-5), 357–371. https://doi.org/10.2113/gssgfbull.184.4-5.357

Lehner, F. K. (1986). Comments on "noncohesive critical Coulomb wedges: An exact solution" by F. A. Dahlen. *Journal of Geophysical Research*, *91*(B1), 793–796.

Lohrmann, J., Kukowski, N., Adam, J., & Oncken, O. (2003). The impact of analogue material properties on the geometry, kinematics, and dynamics of convergent sand wedges. *Journal of Structural Geology*, *25*(10), 1691–1711.

Lugeon, M. (1902). Les grandes nappes de recouvrement des Alpes du Chablais et de la Suisse. *Bulletin de la Societe Geologique de France*, *4*, 723.

Malavieille, J. (2010). Impact of erosion, sedimentation, and structural heritage on the structure and kinematics of orogenic wedges: Analog models and case studies. *GSA Today*, *20*(1), 4–10.

Malavieille, J., & Konstantinovskaya, E. (2010). Impact of surface processes on the growth of orogenic wedges: Insights from analog models and case studies. *Geotectonics*, *44*(6), 541–558. https://doi.org/10.1134/S0016852110060075

Marone, C. (1995). Fault zone strength and failure criteria. *Geophysical Research Letters*, *22*(6), 723–726. https://doi.org/10.1029/95GL00268

Marone, C., Hobbs, B. E., & Ord, A. (1992). Coulomb constitutive laws for friction: Contrasts in frictional behavior for distributed and localized shear. *Pure and Applied Geophysics PAGEOPH*, *139*(2), 195–214. https://doi.org/10.1007/BF00876327

Mary, B. C. L., Maillot, B., & Leroy, Y. M. (2013). Predicting orogenic wedge styles as a function of analogue erosion law and material softening. *Geochemistry, Geophysics, Geosystems*, *14*, 4523–4543. https://doi.org/10.1002/ggge.20262

Massoli, D., Koyi, H. A., & Barchi, M. R. (2006). Structural evolution of a fold and thrust belt generated by multiple décollements: Analogue models and natural examples from the Northern Apennines (Italy). *Journal of Structural Geology*, *28*(2), 185–199.

Merle, O. (1998). *Emplacement mechanisms of nappes and thrust sheets*. Dordrecht: Kluwer Academic Publisher.

Mourgues, R., & Cobbold, P. R. (2006). Thrust wedges and fluid overpressures: Sandbox models involving pore fluids. *Journal of Geophysical Research*, *111*, B05404. https://doi.org/10.1029/2004JB003441

Mourgues, R., Lacoste, A., & Garibaldi, C. (2014). The Coulomb critical taper theory applied to gravitational instabilities. *Journal of Geophysical Research: Solid Earth*, *119*, 754–765. https://doi.org/10.1002/2013JB010359

Park, J.-O., Fujie, G., Wijerathne, L., Hori, T., Kodaira, S., Fukao, Y., et al. (2010). A low-velocity zone with weak reflectivity along the Nankai subduction zone. *Geology*, *38*(3), 283–286.

Park, J.-O., Tsuru, T., Takahashi, N., Hori, T., Kodaira, S., Nakanishi, A., et al. (2002). A deep strong reflector in the Nankai accretionary wedge from multichannel seismic data: Implications for underplating and interseismic shear stress release. *Journal of Geophysical Research*, *107*(B4), 2061. https://doi.org/10.1029/2001JB000262

Pons, A., & Mourgues, R. (2012). Deformation and stability of over-pressured wedges: Insight from sandbox models. *Journal of Geophysical Research*, *117*, B09404. https://doi.org/10.1029/2012JB009379

Ranero, C. R., Grevemeyer, I., Sahling, H., Barckhausen, U., Hensen, C., Wallmann, K., et al. (2008). Hydrogeological system of erosional convergent margins and its influence on tectonics and interplate seismogenesis. *Geochemistry, Geophysics, Geosystems*, *9*, Q03S04. https://doi.org/10.1029/2007GC001679

Reches, Z., & Dewers, T. A. (2005). Gouge formation by dynamic pulverization during earthquake rupture. *Earth and Planetary Science Letters*, *235*(1-2), 361–374.

Ruh, J. B., Kaus, B. J. P., & Burg, J.-P. (2012). Numerical investigation of deformation mechanics in fold-and-thrust belts: Influence of rheology of single and multiple décollements. *Tectonics*, *31*, TC3005. https://doi.org/10.1029/2011TC003047

Ruina, A. (1983). Slip instability and state variable friction laws. *Journal of Geophysical Research*, *88*(B12), 10,359–10,370. https://doi.org/10.1029/JB088iB12p10359

Saffer, D. M., & Tobin, H. J. (2011). Hydrogeology and mechanics of subduction zone forearcs: Fluid flow and pore pressure. *Annual Review of Earth and Planetary Sciences*, *39*(1), 157–186.

Sage, F., Collot, J. Y., & Ranero, C. R. (2006). Interplate patchiness and subduction-erosion mechanisms: Evidence from depth-migrated seismic images at the central Ecuador convergent margin. *Geology*, *34*(12), 997–1000.

Scholl, D. W., Marlow, M. S., & Cooper, A. K. (1977). Sediment subduction and offscraping at Pacific margins. In M. Talwani, & W.C. Pitman (Eds.), *Island arcs, deep sea trenches and back-arc basins* (pp. 199–210). Washington, DC: American Geophysical Union.

Schreurs, G., Buiter, S. J. H., Boutelier, J., Burberry, C., Callot, J.-P., Cavozzi, C., et al. (2016). Benchmarking analogue models of brittle thrust wedges. *Journal of Structural Geology*, *92*, 116–139.

Scott, D. R., Marone, C. J., & Sammis, C. G. (1994). The apparent friction of granular fault gouge in sheared layers. *Journal of Geophysical Research*, *99*(B4), 7231–7246. https://doi.org/10.1029/93JB03361

Selzer, C., Buiter, S. J. H., & Pfiffner, O. A. (2007). Sensitivity of shear zones in orogenic wedges to surface processes and strain softening. *Tectonophysics*, *437*(1-4), 51–70.

Simpson, G. D. H. (2010). Formation of accretionary prisms influenced by sediment subduction and supplied by sediments from adjacent continents. *Geology*, *38*(2), 131–134.

Terzaghi, K. (1950). Mechanism of landslides. *In Application of geology to engineering practice.* Geological Society of America. https://doi.org/10.1130/Berkey.1950.83

Tesei, T., Lacroix, B., & Collettini, C. (2015). Fault strength in thin-skinned tectonic wedges across the smectite-illite transition: Constraints from friction experiments and critical tapers. *Geology*, *43*(10), 923–926.

Tobin, H. J., Moore, J. C., & Moore, G. F. (1994). Fluid pressure in the frontal thrust of the Oregon accretionary prism: Experimental constraints. *Geology*, *22*(11), 979.

van Hinsbergen, D. J. J., Hafkenscheid, E., Spakman, W., Meulenkamp, J. E., & Wortel, R. (2005). Nappe stacking resulting from subduction of oceanic and continental lithosphere below Greece. *Geology*, *33*(4), 325.

Verbosio, F., Coninck, A. D., Kourounis, D., & Schenk, O. (2017). Enhancing the scalability of selected inversion factorization algorithms in genomic prediction. *Journal of Computational Science*, *22*(Supplement C), 99–108. https://doi.org/10.1016/j.jocs.2017.08.013

Vermeer, P. A., & De Borst, R. (1984). Non-associated plasticity for soils, concrete and rock thermo-mechanical behaviour of fibre metal laminates view project HER. *Heron*, *29*(3), 1–64.

von Huene, R., & Ranero, C. R. (2003). Subduction erosion and basal friction along the sediment-starved convergent margin off Antofagasta, Chile. *Journal of Geophysical Research*, *108*(B2), 2079. https://doi.org/10.1029/2001JB001569

von Huene, R., Ranero, C. R., & Vannucchi, P. (2004). Generic model of subduction erosion. *Geology*, *32*(10), 913.

von Huene, R., & Scholl, D. W. (1991). Observations at convergent margins concerning sediment subduction, subduction erosion, and the growth of continental crust. *Reviews of Geophysics*, *29*(3), 279–316.

Vrolijk, P., & van der Pluijm, B. A. (1999). Clay gouge. *Journal of Structural Geology*, *21*(8-9), 1039–1048.

Wang, K., He, J., & Hu, Y. (2006). A note on pore fluid pressure ratios in the Coulomb wedge theory. *Geophysical Research Letters*, *33*, L19310. https://doi.org/10.1029/2006GL027233

Wang, K., & Hu, Y. (2006). Accretionary prisms in subduction earthquake cycles: The theory of dynamic Coulomb wedge. *Journal of Geophysical Research*, *111*, B06410. https://doi.org/10.1029/2005JB004094

Wang, K., Hu, Y., von Huene, R., & Kukowski, N. (2010). Interplate earthquakes as a driver of shallow subduction erosion. *Geology*, *38*(5), 431–434.

Willett, S. D. (1992). Dynamic and kinematic growth and change of a Coulomb wedge, *Thrust tectonics* (pp. 19–31). Dordrecht: Springer Netherlands.

Willett, S. D. (1999). Orogeny and orography: The effects of erosion on the structure of mountain belts. *Journal of Geophysical Research*, *104*(B12), 28,957–28,981. https://doi.org/10.1029/1999JB900248